

**Department of Physics and Astronomy**  
**University of Heidelberg**

Bachelor thesis in Physics

submitted by

**Lorenz Thielbeer**  
born in Köln (Germany)

**2021**



# **Semi-Analytic**

## **Common-Envelope Simulations**

This Bachelor thesis has been carried out by Lorenz Thielbeer at the  
Heidelberg Institute for Theoretical Studies gGmbH  
under the supervision of  
Dr. Fabian Schneider  
and  
Prof. Dr. Friedrich Röpke



### **(Semi-Analytische Gemeinsame-Hülle Simulationen - deutsch):**

Gemeinsame-Hülle (GH) Phasen sind wichtige Ereignisse in der Entwicklung eines Doppelsternsystems und werden üblicherweise mit komplexen dreidimensionalen (3D) Simulationen untersucht. Diese Simulationen benötigen typischerweise mehrere Hunderttausend CPU-Stunden um eine komplette GH-Phase abzudecken. Das Ziel dieser Arbeit ist es herauszufinden, ob es möglich ist, ein semi-analytisches Modell an eine entsprechende 3D-Simulation zu kalibrieren, so dass wir die GH-Phase eines anderen Binärsystems mit hoher Genauigkeit in einer Dimension (1D) simulieren können.

Unter Verwendung der MESA-Profilen zweier Primärsterne lösen wir die Bewegungsgleichung des Begleiters für kreisförmige Bahnen mit einer zusätzlichen Reibungskraft. Mit entsprechenden 3D-Simulationen sind wir in der Lage, Reibungskoeffizienten  $C_d$  zu finden, mit denen wir den Verlauf eines GH-Ereignisses mit unserer semi-analytischen Simulation für mehrere Massenverhältnisse  $q$  folgen können. Allerdings sind die Reibungskoeffizienten für verschiedene Massenverhältnisse nicht konstant. Außerdem finden wir, dass die anfängliche Wahl der Co-Rotation im Binärsystem nicht den Ausgang der GH-Phase ändert, sondern nur die Zeitskala auf der das Event stattfindet. Durch die Verwendung von Reibungsformalismen, die sowohl auf Bondi-Hoyle-Lyttleton Akkretion als auch auf dynamischer Reibung basieren, wird deutlich, dass im Rahmen von GH-Phasen dynamische Reibung besser anwendbar ist als Bondi-Hoyle-Lyttleton Akkretion.

### **(Semi-Analytic Common-Envelope Simulations - english):**

Common envelope (CE) phases are important events in the evolution of a binary system and are usually studied using complex three-dimensional (3D) simulations. These simulations typically require several hundred thousand CPU-hours to cover a complete CE phase. The goal of this thesis is to find out whether it is possible to calibrate a semi-analytic model to a corresponding 3D simulation such that we can simulate the CE phase of a different binary system with high accuracy in one dimension (1D).

Using the MESA profiles of two primary stars, we solve the equation of motion of the companion for circular orbits with an additional drag force. With corresponding 3D simulations we are able to find drag coefficients  $C_d$  to match the course of a CE event with our semi-analytic simulation for multiple mass ratios  $q$ . However, the drag coefficients are not constant for different mass ratios. We also find that the initial choice of co-rotation in the binary system does not change the outcome of the CE phase but only the timescale on which the event takes place. By using drag formalisms based on both Bondi-Hoyle-Lyttleton accretion and dynamical friction, it becomes apparent that, in the framework of CE phases, dynamical friction is more applicable than Bondi-Hoyle-Lyttleton accretion.



# Contents

<b>1</b>	<b>Introduction</b>	<b>9</b>
1.1	Common-Envelope-Phase . . . . .	9
1.2	Bondi-Hoyle-Lyttleton Accretion . . . . .	10
1.2.1	MacLeod Model . . . . .	11
1.3	Dynamical Friction . . . . .	12
1.3.1	Ostriker Model . . . . .	12
1.3.2	Kim and Kim Model . . . . .	13
1.3.3	Kim Model . . . . .	14
<b>2</b>	<b>Methods</b>	<b>16</b>
2.1	Setup . . . . .	16
2.2	Simulation . . . . .	19
2.3	Calibration . . . . .	20
2.4	Analysis . . . . .	20
<b>3</b>	<b>Results</b>	<b>23</b>
3.1	Bondi-Hoyle-Lyttleton Accretion . . . . .	23
3.1.1	MacLeod . . . . .	27
3.2	Dynamical Friction . . . . .	32
3.2.1	Ostriker . . . . .	32
3.2.2	Kim and Kim . . . . .	35
3.2.3	Kim . . . . .	38
3.3	Role of Initial Co-Rotation . . . . .	40
3.4	Final Separation . . . . .	42
<b>4</b>	<b>Discussion</b>	<b>46</b>
4.1	Assumption of Constant Density . . . . .	46
4.2	Hydrodynamic Drag vs. Dynamical Friction . . . . .	47
4.3	The Role of Co-Rotation . . . . .	48
4.4	Outcome of a Common Envelope Event . . . . .	48
<b>5</b>	<b>Conclusion and Outlook</b>	<b>50</b>
<b>6</b>	<b>Acknowledgments</b>	<b>53</b>
<b>A</b>	<b>Additional Figures</b>	<b>54</b>
<b>B</b>	<b>Lists</b>	<b>60</b>
B.1	List of Figures . . . . .	60

B.2	List of Tables	62
<b>C</b>	<b>Bibliography</b>	<b>63</b>

# 1 Introduction

## 1.1 Common-Envelope-Phase

In our galaxy, the Milky Way, only about half of all stars are single like our sun (Lada, 2006). All the other stars are in systems of two or more. In systems of two stars that are orbiting each other, a so-called binary system, common envelope phases can occur. These phases are short episodes in the life of two stars where the cores of the stars orbit each other inside the envelope of one of them. Paczynski (1976) was the first to propose such common envelope phases but since then many more contributed to a better understanding of these events. A more modern review of the current state of research in that field was published by Ivanova et al. (2013).

Usually the two stars have different masses. We call the more massive one primary star, or primary, and the less massive one its companion. While the companion orbits the core of the primary inside its envelope, it is subjected to friction. This friction transforms orbital energy of the companion into heat, which causes the orbital velocity of the two objects to shrink while also expanding the primary's envelope. If enough orbital energy is available, the envelope can also be ejected. In this case, only the core of the primary star remains in close orbit with the companion. Possible phenomena that can arise from common envelope phases include Type Ia supernovae (Iben & Tutukov, 1984; Ruiter et al., 2009), classical novae (Livio et al., 1990), white-dwarf mergers (Pakmor et al., 2010; Ruiter et al., 2013), gravitational wave sources (Belczynski et al., 2002) and also planetary nebulae (de Kool, 1990; Nordhaus et al., 2007; Bermúdez-Bustamante et al., 2020).

Because common envelope phases are fundamentally important events for a range of phenomena, many efforts have been made to study them in great detail, especially with the help of numerical simulations. However, three-dimensional (3D) simulations have to cover a wide range of spatial scales to achieve sufficient resolution. All of the relevant physics need to be covered and evolved from the stellar core up to the surface of the primary star. Modern 3D techniques range from adaptive mesh refinement (Ricker & Taam, 2008, 2012; Taam & Ricker, 2010; Passy et al., 2012) over moving mesh simulations (Ohlmann et al., 2016) to smooth particle hydrodynamics (Nandez et al., 2015; Pejcha et al., 2016a,b). Although, some of them may not even include all the necessary physics, 3D simulations typically require several hundred thousand CPU-hours to cover a complete common envelope phase. Semi-analytic simulations in one dimension (1D), on the other hand, can be carried out in minutes on an ordinary computer.

Soon after it's conception in Paczynski (1976), common envelope phases were already studied using numerical hydrodynamics in 1D (Taam et al., 1978; Meyer &

Meyer-Hofmeister, 1979; Taam, 1979). Simulations like this take hours up to days on a single CPU, albeit being in 1D. These studies showed promising results, however, it was soon found that the resulting evolution was not spherically symmetric. This led to a abandonment of 1D simulations for over 15 years, instead using 3D simulations to account for nonaxisymmetric geometry and turbulent processes. Podsiadlowski (2001) was one of the first to re-introduce 1D simulations of common envelope phases, shortly followed by Ivanova (2002) and more recently by Ivanova & Nandez (2016), Clayton et al. (2017) and Fragos et al. (2019). In this work we will try to match the results of the 3D simulations by Kramer et al. (2020) and Sand et al. (2020) with a semi-analytic 1D simulation. The semi-analytic approach consists in assuming a drag force that is exerted on the companion, in addition to gravity, as it moves through the primary's envelope. The equation of motion is then numerically solved for both objects in the center of mass reference frame. If it is possible to calibrate our semi-analytic simulations to the results from AREPO with a constant calibration factor, significant savings in computation time could be achieved. This is because our 1D simulations are far less demanding than 3D simulations. The calibration will be done by introducing a drag coefficient  $C_d$  by which the drag force in the semi-analytic simulations is multiplied. This coefficient is fitted by minimizing  $\chi^2$  between semi-analytic and AREPO simulation. If the used drag formalism is capable of simulating the in-spiral of the common envelope phase, the determined  $C_d$  should be constant for different mass ratios. If the  $C_d$  are not constant, that implies that the drag formalism is not scaling correctly with the companion's mass and some assumptions of the formalism are not met.

This thesis will start by presenting the formalisms by Bondi-Hoyle-Lyttleton (Edgar, 2004), Ostriker (1999); Kim & Kim (2007) and Kim (2010), which are used to describe the exerted drag force, in Section 1.2, Section 1.3.1, Section 1.3.2 and Section 1.3.3 respectively. In Chapter 2 we will explain the numerical methods used for our semi-analytic simulations. The results we obtain with these methods are then presented in Chapter 3. In Chapter 4 we discuss the results in light of the current state of research and also compare them to work done by others. A summary of the thesis as well as an outlook for the future of this project will be given in Chapter 5.

## 1.2 Bondi-Hoyle-Lyttleton Accretion

Over many years, Bondi, Hoyle and Lyttleton studied the question of how much material a point mass accretes when it is moving linearly through a uniform gas cloud. Edgar (2004) puts the results of the work done by these three together into one review paper. The drag force  $F_{\text{drag}}$  there is described by

$$F_{\text{drag}} = \pi R_a^2 \rho (v_{\text{rel}}^2 + c_s^2)^{1/2} v_{\text{rel}} \quad (1.1)$$

where  $\rho$  is the density of the gas at the current point in the ambient medium,  $v_{\text{rel}}$  is the relative velocity of the companion in the gas and  $c_s$  is the sound speed at the

current point.  $R_a$  is the Bondi accretion radius, which specifies up to which radius from the point particle mass is gravitationally bound to it when the point particle moves at a certain velocity. It is defined as follows,

$$R_a = \frac{2GM_2}{v_{\text{rel}}^2 + c_s^2}, \quad (1.2)$$

where  $G$  is the gravitational constant and  $M_2$  is the mass of the companion. Additionally, we multiply the drag force by a drag calibration factor  $C_d$  which will be important to match the results of the 3D simulations with AREPO. The drag force in a Bondi-Hoyle-Lyttleton framework then finally is

$$F_{\text{drag}} = C_d \frac{4\pi G^2 M_2^2 \rho v_{\text{rel}}}{(v_{\text{rel}}^2 + c_s^2)^{3/2}}. \quad (1.3)$$

### 1.2.1 MacLeod Model

In [MacLeod & Ramirez-Ruiz \(2015\)](#), the authors follow a similar approach as this thesis and try to fit a drag force described by Bondi-Hoyle-Lyttleton accretion to 3D simulations. For this, they set up a wind tunnel experiment where a point particle moves linearly through a gas with a radial density gradient in 3D. They then use the drag force from Bondi-Hoyle-Lyttleton accretion theory and compare it to the drag force found in the 3D simulation in order to obtain drag calibration coefficients. However, they define the drag force slightly differently than Eq. (1.3) and don't use the sound speed in the formula. Their drag force is

$$F_{\text{drag}} = C_d \frac{4\pi G^2 M_2^2 \rho}{v_{\text{rel}}^2}. \quad (1.4)$$

For the formula they want to fit the  $C_d$  to, they also define a density scale height as

$$H_\rho = -\rho \frac{dr}{d\rho} \quad (1.5)$$

where  $dr/d\rho$  is the derivative of the orbital separation between companion and primary to the density. Additionally they define a dimensionless parameter which expresses the number of density scale heights removed by the accretion radius

$$\epsilon_\rho = \frac{R_a}{H_\rho}. \quad (1.6)$$

Also here, the accretion radius does not contain the sound speed, as it did before, and is instead defined as

$$R_a = \frac{2GM}{v_{\text{rel}}^2}. \quad (1.7)$$

The formula they fitted the found drag coefficients to finally is

$$C_d = c_1 + c_2 \epsilon_\rho + c_3 \epsilon_\rho^2 \quad (1.8)$$

and the fitting parameters are  $c_i = (1.98255197, -1.33691133, 0.62963326)$ . This formula will later be used to provide the  $C_d$  for our semi-analytic simulation and we will compare the results to a corresponding 3D simulation in AREPO.

## 1.3 Dynamical Friction

Another idea to describe drag is that it does not apply as a form of wind pressing against the object but instead arises from gravitational focusing of material behind the object. The object, in our case the companion, is then gravitationally attracted by the focused material behind it and therefore experiences a drag force. This problem, called dynamical friction, was first studied by [Chandrasekhar \(1943\)](#) for the case of a collisionless medium through which the object travels. The case of a gaseous (i.e. collisional) medium was discussed by [Dokuchaev \(1964\)](#), [Ruderman & Spiegel \(1971\)](#) and [Rephaeli & Salpeter \(1980\)](#). The estimated drag force in a steady supersonic case was proposed to be

$$F_{\text{drag}} = \frac{4\pi(GM_2)^2\rho}{v_{\text{rel}}^2} \ln\left(\frac{r_{\max}}{r_{\min}}\right) \quad (1.9)$$

where  $\ln(r_{\max}/r_{\min})$  is called Coulomb logarithm.  $r_{\max}$  and  $r_{\min}$  are the effective linear sizes of the ambient medium (here the primary) and the perturber (here the companion) respectively. However their choices remain somewhat ambiguous. Many studied these parameters but in this thesis we focus on the work done by [Ostriker \(1999\)](#), [Kim & Kim \(2007\)](#) and [Kim \(2010\)](#) and will use their results for our semi-analytic simulations.

### 1.3.1 Ostriker Model

In their work, [Ostriker \(1999\)](#) extended the work of [Rephaeli & Salpeter \(1980\)](#) for subsonic motion of the companion and found the drag force to be

$$F_{\text{drag}} = C_d \frac{4\pi(GM_2)^2\rho}{v_{\text{rel}}^2} I \quad (1.10)$$

where  $C_d$ , again, is the drag coefficient we will use to match this formula to the drag force present in AREPO.  $I$  is their definition of the Coulomb logarithm. For the subsonic regime they found

$$I_{\text{subsonic}} = \frac{1}{2} \ln\left(\frac{1+\mathcal{M}}{1-\mathcal{M}}\right) - \mathcal{M} \quad (1.11)$$

where  $\mathcal{M} = v_{\text{rel}}/c_s$  is the Mach number (subsonic:  $\mathcal{M} < 1$ ). For supersonic motion, i.e.  $\mathcal{M} > 1$ , the Coulomb logarithm is

$$I_{\text{supersonic}} = \frac{1}{2} \ln \left( 1 - \frac{1}{\mathcal{M}^2} \right) + \ln \left( \frac{r_{\max}}{r_{\min}} \right). \quad (1.12)$$

Here, we deviate slightly from the definition in Ostriker (1999) as we use  $r_{\max} = 2 \cdot r$ , where  $r$  is the separation between the companion and the core of the primary. They use  $r_{\max} = v_{\text{rel}} \cdot t$ , which describes the displacement of the perturber to its original position. This is because in Ostriker (1999), the perturber moves on a linear trajectory. However, we use same definition of  $r_{\min}$  which describes the effective size of the companion. In the models of Kramer et al. (2020) and Sand et al. (2020) this size is given by the so-called softening length and has a value of  $r_{\min} = 3.1 R_\odot$  for both models.

### 1.3.2 Kim and Kim Model

Previous studies, including Ostriker (1999), strictly apply to a massive object that travels through an infinite homogeneous background on a straight-line trajectory. However, many astrophysical problems like common envelope phases follow circular or near-circular orbits. This is why Kim & Kim (2007) studied the effect of circular orbits on the wake of the companion and thus the drag force it is subjected to. Also using Eq. (1.10), they found the following Coulomb logarithms.

$$I = \begin{cases} 0.7706 \ln \left( \frac{1+\mathcal{M}}{1.0004-0.9185\mathcal{M}} \right) - 1.4703\mathcal{M}, & \text{for } \mathcal{M} < 1.0 \\ \ln [330(r/r_{\min})(\mathcal{M} - 0.71)^{5.72}\mathcal{M}^{-9.58}], & \text{for } 1.1 \leq \mathcal{M} < 4.4 \\ \ln [(r/r_{\min})/(0.11\mathcal{M} + 1.65)], & \text{for } 4.4 \leq \mathcal{M} \end{cases} \quad (1.13)$$

where  $r$  is the orbital separation between companion and primary and, as before,  $r_{\min} = 3.1 R_\odot$  for both of the used models.

Numerical simulations showed that the drag force on circular orbits is smaller for supersonic motion than predicted by the estimate of Ostriker (1999) (see Sánchez-Salcedo & Brandenburg, 2001; Escala et al., 2004). This is due to the companion passing through its own wake, which cannot happen on a straight-line trajectory. A comparison of the formalisms by Bondi, Hoyle and Lyttleton, Ostriker (1999) and Kim & Kim (2007) can be found in Figure 1.1. It shows that, indeed, the found Coulomb logarithm by Kim & Kim (2007) results in a lower drag force for Mach numbers greater than two. This indicates that, by construction, this formalism might be better suited for our semi-analytic simulations. The results will show that this is indeed the case. The plot is similar to Figure 8 in Kim & Kim (2007) but additionally includes the Bondi-Hoyle-Lyttleton formalism which was plotted using Eq. (1.4). It is visible that the Bondi-Hoyle-Lyttleton formalism returns a lower drag force than the dynamical friction formalisms for Mach numbers greater than one and

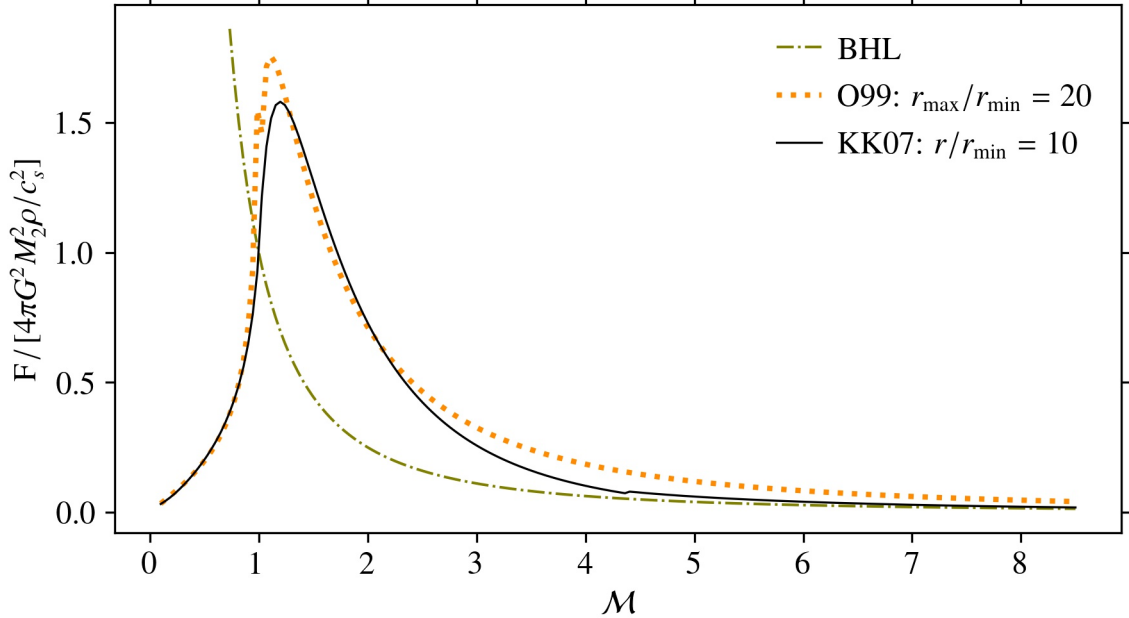


**Figure 1.1:** Exerted drag force on a companion that travels through a gaseous medium as function of Mach number. The formalism of Kim & Kim (2007) is plotted as a black solid line and is in good agreement with the formalism of Ostriker (1999) which is plotted as orange dotted line. Additionally, the Bondi-Hoyle-Lyttleton formalism is plotted as green dashed-dotted line.

increases proportional to  $\mathcal{M}^2$  for  $\mathcal{M} \rightarrow 0$ . These two features will be important for our semi-analytic simulations and will be the reason why the Bondi-Hoyle-Lyttleton formalism is not well suited for our approach. This will be most evident for more massive companions where the perturbation becomes non-linear and Mach numbers decrease below one.

### 1.3.3 Kim Model

Kim (2010) further extended their previous work to study the effect of significantly more massive companions on circular orbits. In this case the linear perturbation theory, which was applied in all of the previously discussed works, does not hold anymore. In order to describe the drag force in a non-linear case, the author introduces the dimensionless parameter

$$\mathcal{B} = \frac{GM_2}{c_s^2 r} \quad (1.14)$$

which is the Bondi accretion radius in units of the orbital separation of companion

and primary. Further, they define

$$\eta_B = \frac{B}{M^2 - 1} \quad (1.15)$$

which will be used to determine if the companion is in a linear or non-linear regime. More specifically, [Kim \(2010\)](#) found that non-linear perturbation applies if  $\eta_B > 0.1$ . Since in the non-linear case it is inevitable for the companion to enter the backside of its own wake due to the circular orbit, the author also considers a change in density as follows.

$$\rho_{nl} = \left( 1 + \frac{0.46B^{1.1}}{(M^2 - 1)^{0.11}} \right) \rho \quad (1.16)$$

where  $\rho$  is the density in the linear case. The drag force for non-linear perturbation by massive companions then finally is

$$F_{drag} = C_d \frac{4\pi\rho_{nl}(GM_2)^2}{v_{rel}^2} \left( \frac{0.7}{\eta_B^{0.5}} \right), \text{ for } \eta_B > 0.1. \quad (1.17)$$

It is to note that for our semi-analytic simulations we introduce the additional condition that in the non-linear case the Mach number must be greater than 1.01, i.e.  $M > 1.01$ . This is necessary because  $\rho_{nl} \rightarrow \infty$  for  $M \rightarrow 1$ . Without this limitation,  $F_{drag}$  would approach infinity if  $M$  comes close to one.

In the simulations where we use this formalism for non-linear perturbation by massive companions, we also use the formalism by [Kim & Kim \(2007\)](#) for the linear cases during the simulation, i.e. for  $\eta_B \leq 0.1$  or  $M \leq 1.01$ .

## 2 Methods

This chapter covers the setup of the semi-analytic simulations. We will derive the used equations of motion and other quantities like distances and velocities in the center of mass reference frame. Furthermore, all the numerical methods that were used during the simulations, for analysis as well as for calibration, will be explained.

### 2.1 Setup

First, we derive the equation of motion for both the primary star (denoted with subscript 1 in the following) and the companion (denoted with subscript 2). We describe the binary system in the non-rotating center of mass reference frame of the two objects. Due to the absence of rotation of the frame, we do not have any inertial (or pseudo) forces like centrifugal or Coriolis force. Therefore, the only force the primary star is subjected to is the gravitational force,

$$F_1 = F_g = -\frac{GM_1M_2}{r^2}. \quad (2.1)$$

Where  $M_1$  is the mass of the primary star,  $M_2$  is the companion's mass and  $r = r_1 + r_2$  is the orbital separation between  $M_1$  and  $M_2$  with  $r_1$  and  $r_2$  being the distances of primary and companion to their shared center of mass.

The companion is additionally subjected to a drag force that is acting in opposite direction to the motion of the companion. This drag force is exerted by the gas of the primary's envelope and will be described by the four different formulas discussed in the introduction. Because of this, the drag force will just be given as  $F_d$  for the entirety of this chapter. Thus, the total force acting on the companion is

$$F_2 = F_g + F_d = -\frac{GM_1M_2}{r^2} + F_d. \quad (2.2)$$

Utilizing Newton's second law of motion  $F = m \cdot a$ , where  $m$  is the object's mass and  $a$  the acceleration it experiences, the equations of motion then follow with

$$\ddot{r}_1 = -\frac{GM_2}{r^2}, \quad (2.3)$$

$$\ddot{r}_2 = -\frac{GM_1}{r^2} + F_d/M_2. \quad (2.4)$$

By introducing  $v = dr/dt$ , we obtain a set of first order differential equations.

$$\frac{dr_1}{dt} = v_1, \quad (2.5)$$

$$\frac{dv_1}{dt} = -\frac{GM_1}{r^2}, \quad (2.6)$$

$$\frac{dr_2}{dt} = v_2, \quad (2.7)$$

$$\frac{dv_2}{dt} = -\frac{GM_1}{r^2} + F_d/M_2. \quad (2.8)$$

These will be solved using a numerical Runge-Kutta solver, which will be discussed in more detail in Section 2.2.

For the gravitational force acting on the companion, the enclosed mass for each radius, i.e. the mass of the primary inside of a certain radius from its core, is needed. The drag force depends on the density of the envelope and the speed of sound at any radius. Both the  $0.76 M_\odot$  RGB (Kramer et al., 2020) and  $0.97 M_\odot$  AGB (Sand et al., 2020) primary stars were evolved from a zero-age main sequence star to their current state with the stellar evolution code MESA (Paxton et al., 2011). For solving the equations of motion, the needed stellar properties of the primary are therefore provided by the corresponding MESA profile and have been evaluated at a wide range of radii from the primary's core. A linear interpolation is then used to obtain functions of radius for all of these quantities. Since the data sets provided by MESA already have a high resolution, a linear interpolation is sufficient here. The interpolation is also set up to return the last value of the corresponding MESA data set if the argument is outside the limits of the radius data. The companion, on the other hand, is a point particle of constant mass without further properties.

The initial conditions of the semi-analytic common envelope simulation are then chosen to be as close as possible to the initial conditions in the corresponding AREPO simulation. With this, we aim for maximum comparability. The initial separation between primary and companion is taken directly from the corresponding AREPO output. For the  $0.97 M_\odot$  primary star, the companion starts outside of the primary's envelope in AREPO. Here, we use the radius of the primary as initial separation to ensure that the companion is exposed to the drag force from the beginning of the semi-analytic simulation.

Next, the initial velocities of primary and companion need to be determined. In the center of mass reference frame, we defined earlier that  $r_1$  is the distance of the primary to the center of mass and  $M_1$  is the mass of the primary.  $r_2$  and  $M_2$  are the corresponding quantities for the companion and  $r = r_1 + r_2$  is the separation between primary and companion. Therefore, we have

$$r_2 M_2 = r_1 M_1 \quad (2.9)$$

$$\Rightarrow r_2 M_2 = (r - r_2) M_1 \quad (2.10)$$

$$= r M_1 - r_2 M_1 \quad (2.11)$$

$$\Leftrightarrow r_2(M_1 + M_2) = r M_1 \quad (2.12)$$

$$\Leftrightarrow r_2 = \frac{M_1}{M_1 + M_2} r \quad (2.13)$$

and analogously follows

$$r_1 = \frac{M_2}{M_1 + M_2} r. \quad (2.14)$$

Following the derivation of Kepler's third law by setting gravity equal to the centripetal force, we can derive the orbital velocity of the companion for circular orbits,

$$\Rightarrow \frac{GM_1 M_2}{r^2} = M_2 \omega^2 r_2 = M_2 \frac{v_2^2}{r_2} \quad (2.15)$$

$$\Leftrightarrow v_2^2 = \frac{GM_1 r_2}{r^2} = \frac{GM_1^2}{r(M_1 + M_2)}. \quad (2.16)$$

Analogously, we find for the orbital velocity of the primary star

$$v_1^2 = \frac{GM_2^2}{r(M_1 + M_2)}. \quad (2.17)$$

Finally, the initial co-rotation is also set up to be identical to AREPO. There, the constant angular velocity at which the envelope rotates as a solid body is defined to be 95% of the companion's velocity at the initial separation of primary and companion. The initial separation in AREPO is defined to be a certain percentage of the separation given by the effective radius  $r_L$  of the Roche lobe. In Kramer et al. (2020) this is 80%, while in Sand et al. (2020) it is 60%. The effective radius of the Roche Lobe is calculated by an approximation formula (Eggleton, 1983)

$$r_L = \frac{R_L}{r} = \frac{0.49(\frac{1}{q})^{2/3}}{0.6(\frac{1}{q})^{2/3} + \ln(1 + (\frac{1}{q})^{1/3})} \quad (2.18)$$

where  $R_L$  is the radius of the sphere whose volume approximates the Roche lobe of the heavier object in the binary system, i.e. the primary in our case,  $r$  is the wanted separation of the objects, as defined earlier, and  $q = M_2/M_1$  is their mass

ratio which was defined inversely in Egginton (1983) and is thus used as it's inverse here. The initial separation now follows with

$$r_{\text{ini}} = C_r \cdot a = C_r \frac{R_L}{r_L} = C_r \frac{R_1}{r_L} \quad (2.19)$$

where  $C_r$  is a radius calibration factor that differs between the AREPO simulation and  $R_1$  is the radius of the primary. To obtain the angular velocity in the binary we then use the previously derived formulas for  $v_2$  and  $r_2$  and arrive at Kepler's third law

$$\omega = \frac{v_2}{r_2} = \frac{(M_1 + M_2)}{rM_1} \sqrt{\frac{GM_1^2}{r(M_1 + M_2)}} = \sqrt{\frac{G(M_1 + M_2)}{r^3}}. \quad (2.20)$$

Inserting the initial orbital separation, now gives us the wanted equation for the angular velocity of the primary's envelope

$$\omega_{\text{env}} = f_{\text{corot}} \sqrt{\frac{G(M_1 + M_2)}{r_{\text{ini}}^3}}. \quad (2.21)$$

With this the initial conditions are set up and for the most part they are identical to the setup of the AREPO simulations. The only deviation is the initial separation of the simulations with the  $0.97 M_\odot$  AGB primary star, where  $r_{\text{ini}}$  is chosen to be equal to the radius of the primary. This is a measure to ensure that the companion is subjected to the drag force in the beginning of the semi-analytic simulation. Otherwise it would stay on circular orbits and would never start an in-spiral phase.

## 2.2 Simulation

Solving the equations of motion for primary and companion and simulating their common envelope phase is done by using the Runge-Kutta-Fehlberg method, also known as RK45. This method is well suited for our intentions of semi-analytic simulations because it is a method of order  $O(h^4)$  with an error estimator of order  $O(h^5)$  and allows for adaptive step size. With an adaptive step size, the error of the integration can be controlled and minimized. This is important when our two objects get close to each other because the velocities there are large and even small deviations in the position of the objects would then cause significant changes in the orbital evolution.

Specifically, the function "`solve_ivp`" from the Python library "`scipy`" is used with Eq. (2.5)-(2.8) as time derivatives for each quantity, the discussed initial conditions and a relative accuracy (number of significant digits) of  $\text{rtol} = 10^{-10}$ . The

integration time is set to a multiple of the initial orbital period in order to keep computation time reasonable and still cover a comparable time frame of the in-spiral phase as AREPO. Of course,  $F_d$  is also substituted with one of the discussed drag formalisms in Eq. (2.8) before applying the RK45 method.

## 2.3 Calibration

To calibrate our semi-analytic simulation to the corresponding AREPO simulation, we start by guessing a drag coefficient  $C_d$ . Experience shows that for smaller mass ratios ( $q \leq 0.1$ ) these are usually in the order of unity and smaller than one for higher mass ratios ( $q \geq 0.25$ ). A satisfying  $C_d$  is found, when the slope of the companion's in-spiral is similar to the one returned by AREPO. This is judged by eye. Afterwards, a time offset is guessed, if needed. When a good 'fit-by-eye' was found, we try to minimize  $\chi^2$  between the semi-analytic simulation and AREPO. For this, we follow the formula of Pearson

$$\chi^2 = \sum_{i=1}^n \frac{(O_i - E_i)^2}{E_i} \quad (2.22)$$

where  $n$  is the number of values provided by the AREPO data,  $O_i$  are the observed separations returned by our semi-analytic simulation and  $E_i$  are the expected separation values provided by AREPO, which our simulations is supposed to meet. Since the data set returned by our simulation has more values than the data from AREPO, we interpolate the semi-analytic data to find the corresponding separations for the radii from AREPO. By testing multiple pairs of time offset and  $C_d$ , the smallest  $\chi^2$  is empirically determined. This 'brute force' approach is sufficient in our case because the semi-analytic simulations do not take long to run. Further, we only want to find the best possible fit to the AREPO simulation and not to make any hypothesis testing.

It is to note that we do not use the technique of minimizing  $\chi^2$  for mass ratios  $q \geq 0.25$  within the framework of the first drag formalism. There, we think it makes more sense to match the beginning of the in-spiral, rather than minimizing  $\chi^2$ . This is because the latter would result in the semi-analytic simulation not looking similar to AREPO at all, as the slopes would not match up at any point. Instead we try to calibrate the slope in the beginning of the in-spiral by eye.

## 2.4 Analysis

The solving algorithm returns values for positions and velocities in the  $xy$ -plane of both primary and companion for every evaluated point in time. It does, however, not return values for the forces or accelerations. This is why for analysis and plotting

the results, these quantities are calculated with the returned values. For the other needed stellar properties, again, the MESA data is used.

Gravity is computed as in Eq. (2.1) and the drag force according to the used drag formalism. As a tool for analysis if the common envelope phase was successful or not, i.e. if it reached a final separation or if the objects have merged, the tidal disruption radius is also determined. This is the radius where material from the companion is attracted by the mass of the primary so strongly, that it is no longer bound to the companion. Thus, the companion loses its mass to the primary and the two objects merge. The common envelope phase is then considered to lead to a merger.

In order to compute the tidal disruption radius, we need to assume a radius for the companion, which was originally set up as a point particle. Therefore, we use the observation that brown dwarfs and low-mass stars with masses of  $M_2 \leq 0.1 M_\odot$  all have a very similar radius of about  $R_2 \approx 0.1 R_\odot$  (see e.g. Chabrier et al., 2000). For more massive stars, we use a data set of zero-age main sequence stars with a wide range of masses and radii that have been evolved with the stellar evolution code MESA. The masses and radii are interpolated to obtain a function that takes stellar mass as an argument and returns the radius of the star. The tidal disruption radius  $r_{\text{td}}$  itself (see Shu, 1982, p.431) is then calculated with

$$r_{\text{td}} = R_2 \left( 2 \frac{M_1}{M_2} \right)^{1/3}. \quad (2.23)$$

Further, a variable offset is added to the time, which - just like the drag coefficient  $C_d$  - will be used to calibrate our semi-analytic model to AREPO. This addition is possible, because there is no specific or intrinsic point in time where the in-spiral phase should start. The time at which the in-spiral starts is arbitrary and can be chosen freely in order to find a better fit to AREPO. It is more important that the timescale of the in-spiral phase and the eccentricity of the orbits are similar to AREPO than that the starting point is the same. Especially for the simulations with the  $0.97 M_\odot$  AGB star as a primary, it is important to have an offset in time because we start our simulation at a smaller separation than in AREPO. By doing that, we capture the part of the common envelope phase that takes place within the primary. In AREPO these simulations already start outside of the star radius and only reach the surface of the primary some time later. Therefore, it is necessary to change the starting point of our semi-analytic simulation to keep the comparability to AREPO.

For analysis of the end of the in-spiral phase, we define a timescale that describes how long it takes to remove all of the angular momentum

$$\tau_{\text{in}} = \frac{L_{\text{orb}}}{\dot{L}_{\text{orb}}} \quad (2.24)$$

where  $L_{\text{orb}}$  is the orbital angular momentum and  $\dot{L}_{\text{orb}}$  its time derivative. With the

radii derived earlier and assuming circular orbits, we find

$$L_{\text{orb}} = M_1 r_1^2 \omega + M_2 r_2^2 \omega = M_1 M_2 \sqrt{\frac{Gr}{M_1 + M_2}}. \quad (2.25)$$

The time derivative of  $L_{\text{orb}}$  is given by the torque on  $M_2$  exerted by the drag force

$$\dot{L}_{\text{orb}} = r_2 F_d = \frac{M_1}{M_1 + M_2} r F_d. \quad (2.26)$$

This then gives

$$\tau_{\text{in}} = \frac{M_2}{F_d} \sqrt{\frac{G(M_1 + M_2)}{r}}. \quad (2.27)$$

Utilizing Kepler's third law

$$\frac{P^2}{4\pi^2 r^2} = \frac{r}{G(M_1 + M_2)}, \quad (2.28)$$

where  $P$  is the orbital period, we finally arrive at

$$\tau_{\text{in}} = \frac{M_2}{F_d} \frac{2\pi r}{P}. \quad (2.29)$$

Additionally another timescale

$$\tau = \frac{r}{|\dot{r}P|}, \quad (2.30)$$

defined by [Ivanova & Nandez \(2016\)](#), is used to characterize the end of the in-spiral phase. This timescale describes how long it would take to fully remove the orbital separation between primary and companion in units of the current orbital period. [Ivanova & Nandez \(2016\)](#) propose that the in-spiral of the companion has ended when  $r/|\dot{r}P|$  becomes greater than 10. This limit will be tested with our semi-analytic simulations.

# 3 Results

In this chapter, the results of solving the equation of motion for a companion that is orbiting the core of a more massive RGB or AGB primary star inside the primary's envelope are presented. The equation of motion thereby consists of gravity and an additional drag force that is here described by four different formalisms. The different drag forces will be compared to each other in terms of how well they are suited for describing a common envelope phase. Additionally, the insights that can be gained from our semi-analytic setup about the choice of the initial co-rotation for companion and primary will be shared and explained. Finally we will discuss how the end of the companion's in-spiral phase can be characterized and what the mechanisms behind it are.

## 3.1 Bondi-Hoyle-Lyttleton Accretion

In the following, all the plots that have been used to analyze the different drag formalisms will be explained using the example of a  $0.76 M_{\odot}$  RGB primary star with a  $0.01 M_{\odot}$  companion, i.e. a mass ratio of  $q = M_2/M_1 = 0.01$ , and a drag force that is described by Bondi-Hoyle-Lyttleton accretion.

Figure 3.1 displays the tracks of both the primary star and the companion in the  $xy$ -plane over the course of the common envelope phase. The axes show the distance to the shared center of mass of  $M_1$  and  $M_2$  at  $x = 0$  and  $y = 0$  in solar radii. This type of plot shows the in-spiral phase of the companion and this one in particular already shows that the in-spiral slows down over time, approaching a final separation of primary and companion.

The second standard plot (Figure 3.2) compares the results of solving the equation of motion with only an additional drag force and the results of the corresponding 3D hydro-simulation with AREPO. Additionally, the tidal disruption radius, i.e. the orbital separation where tidal forces would rip the companion apart before it could advance further into the envelope of the primary, is plotted. With this, we check if the semi-analytic solution reaches separations where the two objects would be considered to merge. Also here, the slowing-down of the in-spiral is visible and the similarity of the semi-analytic approach to the 3D-simulation in this first separation plot is already remarkable.

Figure 3.3 shows the relative velocity  $v_{\text{rel}}$  of the companion in the gas of the primary's envelope, the sound speed  $c_s$  at the position of the companion inside the envelope and also the the Mach number  $\mathcal{M} = v_{\text{rel}}/c_s$  at the companion's position for any given time during the semi-analytic simulation. This type of plot is important for the analysis of the in-spiral phase, especially because later drag formalisms strongly

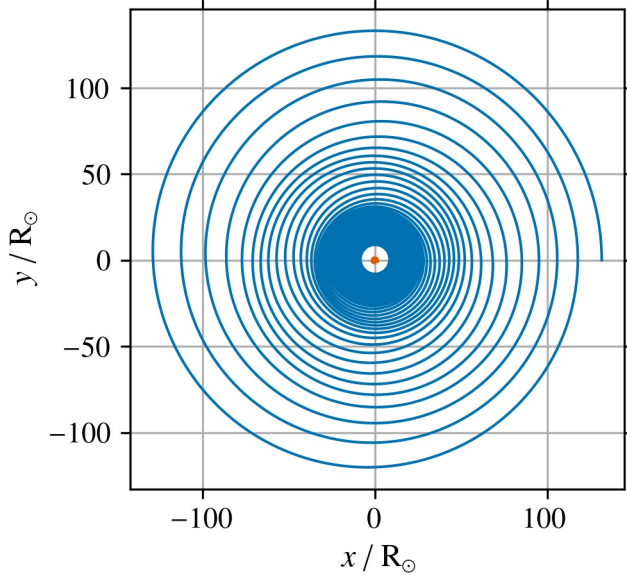


**Figure 3.1:** Position in the  $xy$ -plane of the primary star as orange dotted line (hardly moves because of the small mass ratio) and the companion as blue solid line over the course of the in-spiral phase for  $q = 0.01$  with a drag force described by Bondi-Hoyle-Lyttleton accretion.

depend on the Mach number and whether the companion is in sub- or supersonic motion. We can see that over the course of the in-spiral phase both the relative velocity and the sound speed in the gas of the primary's envelope increase. For the relative velocity  $v_{\text{rel}} = v_{\text{orb}} - v_{\text{env}}$  this is the case because the orbital velocity  $v_{\text{orb}} = \sqrt{GM_1/r}$  increases if the separation  $r$  of companion and primary star decreases while the velocity of the envelope  $v_{\text{env}} = \omega \cdot r$  decreases with decreasing  $r$  (the primary star is assumed to rotate as a solid body rotator, i.e. it has a constant angular velocity at any radius). The sound speed  $c_s$  increases over the course of the in-spiral phase because it depends on the density of the gas which, in a star, increases closer to the core where gravity is strongest. The Mach number  $\mathcal{M} = v_{\text{rel}}/c_s$  does not have a continuously increasing or decreasing course since both of its components increase over time. However, we can say that if  $c_s$  increases faster than  $v_{\text{rel}}$ , the Mach number will decrease and vice versa.

Another plot (Figure 3.4) used for analysis, and also the last type of the standard plots, displays the exerted drag force and gravitational force. Their ratio is also plotted and will be important for the understanding of the end of the in-spiral phase. Generally, we can say that the gravitational force becomes larger with decreasing separation, as one would expect from its dependency  $F_g \propto 1/r^2$ , and  $F_d$  increases more slowly than  $F_g$  although it has more complex dependencies and cannot easily be generalized like  $F_g$  for decreasing separations. This will be explained and discussed in more detail in Section 3.4 on final separations. Here, it is sufficient to note

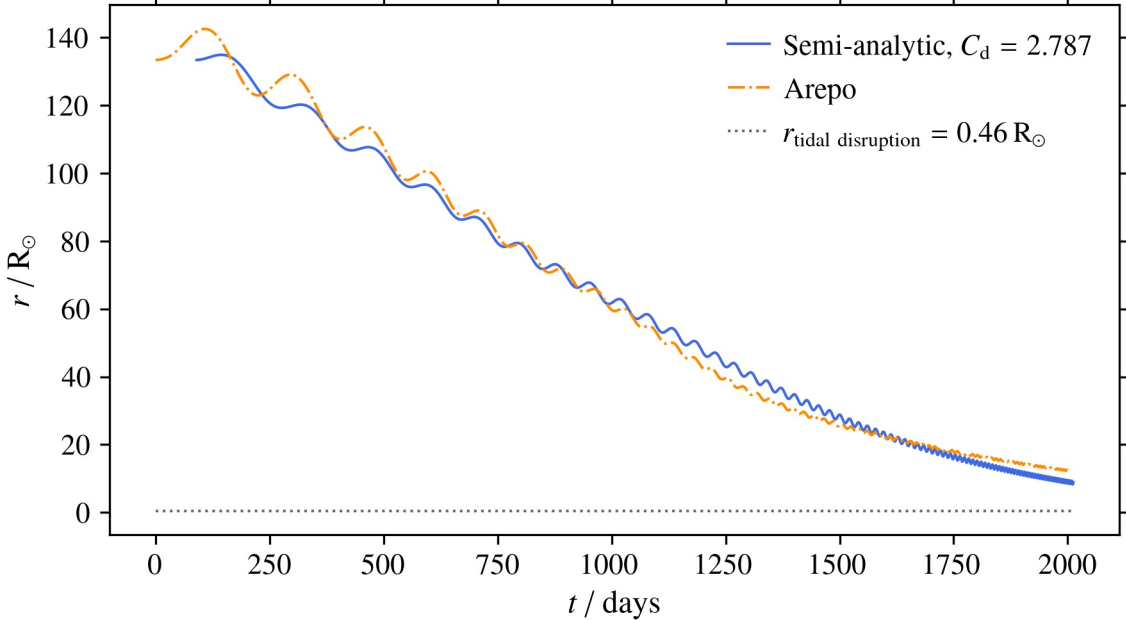


**Figure 3.2:** Separation of primary star and companion for  $q = 0.01$  as a function of time with a drag force described by Bondi-Hoyle-Lyttleton accretion as blue solid line compared to the corresponding 3D-simulation with AREPO as orange dashed-dotted line. The tidal disruption radius is plotted as grey dotted line.

that the ratio  $F_d/F_g$  is approaching zero at the end of the in-spiral phase as the gravitational force becomes larger than the drag force by orders of magnitude. More forces plots, also for other formalisms, can be found in Figure A.1, Figure A.3 and Figure A.5 in the appendix. Both velocity and forces plots will be used to better understand the observed phenomena of in-spiral phase and it's slowing down to a final separation.

Using a drag force that is based on Bondi-Hoyle-Lyttleton accretion, we fit the drag coefficients such that the semi-analytic simulation is as close as possible to the AREPO simulation. We find that for smaller mass ratios  $q$  higher drag coefficients  $C_d$  are needed. For  $q = 0.01\text{--}0.10$ ,  $C_d$  decreases from  $C_d = 2.787$  ( $q = 0.01$ ) to  $C_d = 1.237$  ( $q = 0.10$ ). This decrease indicates that even though the semi-analytic results look remarkably similar to the 3D AREPO simulation (see Figure 3.5), this formalism does not scale correctly with the mass ratio  $q$ . Small deviations in  $C_d$  are to be expected, because the envelope of the primary gets disturbed by the companion and expands as a consequence while decreasing in density. It is not yet fully understood how much the companion changes the structure of the envelope and thus its density but in our semi-analytic simulation this feature is not represented at all. Here, the density of the envelope is assumed to be constant over the course of the common envelope phase. A more massive companion would cause the envelope to expand stronger and result in a more significant change in density. This would lead to a lower drag force.

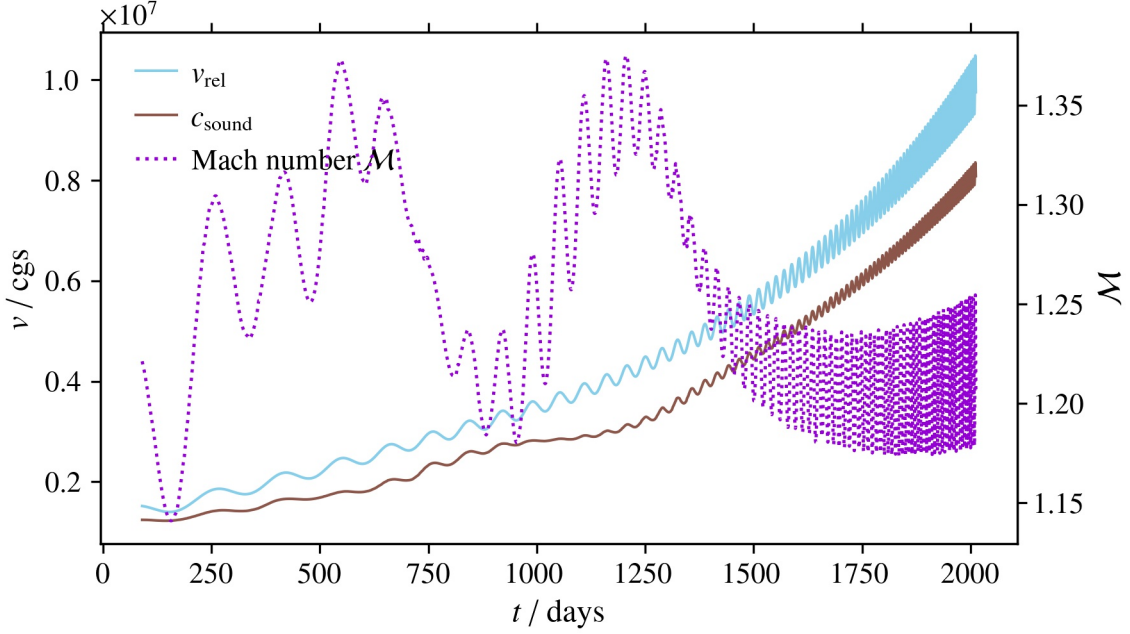


**Figure 3.3:** Relative velocity of the companion in the gas of the envelope as blue solid line, sound speed as brown solid line and Mach number as purple dotted line for  $q = 0.01$  as a function of time with a drag force described by Bondi-Hoyle-Lyttleton accretion.

We would therefore expect to find lower  $C_d$  for higher  $q$  in order to compensate for our assumption of constant density. This assumption may also be the reason why for  $q \leq 0.10$  the semi-analytic simulations do not seem to approach a final separation that is greater than the tidal disruption radius, whereas the AREPO simulations do. The discrepancy between final separations is even bigger for  $q \geq 0.25$ . The semi-analytic simulations for  $q = 0.50$  and  $q = 0.75$  reach final separations greater than the tidal disruption radii. However, these separations are significantly lower than the final separations of the AREPO simulations which, again, is probably due to our assumption that the density in the envelope is constant.

Even though it is to be expected that the drag coefficients change for different  $q$ , a smaller change in  $C_d$  is nevertheless an indicator for a higher quality of the used drag formalism. This is especially true for smaller  $q \leq 0.10$ . There, the disturbance caused by the companion is not as strong as it is for more massive companions. If  $C_d$  was constant for  $q = 0.01-0.10$ , which all have the same primary star and thus the same density profile, the drag force during the in-spiral phase would be well described by the current drag formalism (here Bondi-Hoyle-Lyttleton accretion). We would then only need to calibrate  $C_d$  once in order to match our semi-analytic model to the AREPO simulations. Once found,  $C_d$  would be constant for all binary systems with the same primary since this would imply the same density profile.

In order to make the change in  $C_d$  more tangible and more comparable to later results we plot the results of a semi-analytic simulation for  $q = 0.01$  with the  $C_d$  we

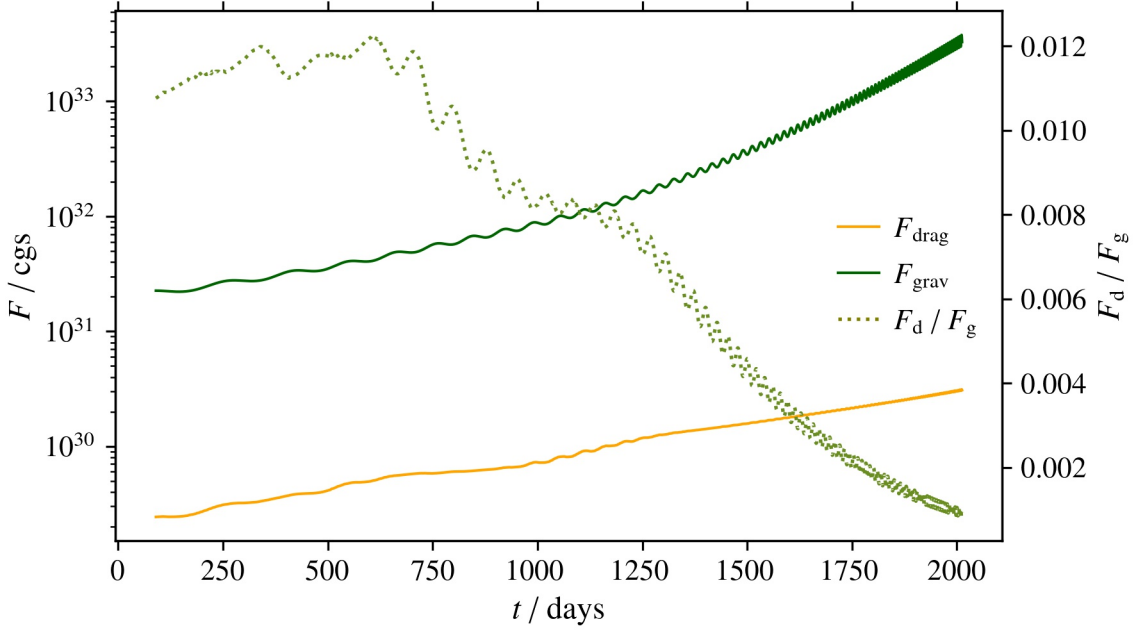


**Figure 3.4:** Drag force as orange solid line, gravitational force as green solid line and their ratio as green dotted line for  $q = 0.01$  as a function of time with a drag force described by Bondi-Hoyle-Lyttleton accretion.

found for  $q = 0.10$  (Figure 3.6). The result for the best fitting  $C_d$  is also plotted, as well as the original AREPO result. Additionally, the AREPO result is plotted with an offset of  $n \cdot r_{\text{fin}}$ , where  $r_{\text{fin}}$  is the last orbital separation in the data set of AREPO and  $n = 1, 2, 3, 4, 5$ . This helps to categorize the quality of the current drag formalism because it reveals how far off the semi-analytic result is when using a  $C_d$  that was found for a higher  $q$ . A better formalism would show a smaller deviation in final separation as it scales more correctly with the companion's mass and therefore would have smaller changes in the found  $C_d$  for different mass ratios.

As we can see in Figure 3.6, the formalism with a drag force that is described by Bondi-Hoyle-Lyttleton accretion does not seem to scale correctly with  $q$ . Otherwise the deviation in final separation of the two semi-analytic simulations would not be as large as it is with  $\Delta r > 4 \cdot r_{\text{fin}}$ . Furthermore, the results for the simulation with  $C_d = 1.237$  (which was originally found for  $q = 0.10$ ) would be closer to the results of the simulation with the best fitting  $C_d$  for the used mass ratio  $q = 0.01$ . For  $q \geq 0.25$  a comparison like this is inconclusive as the  $C_d$  there were fitted by eye and the results are significantly different than the AREPO results. A summary of the determined drag coefficients for all formalisms can be found in Table 3.1.

### 3.1.1 MacLeod

In their work, [MacLeod & Ramirez-Ruiz \(2015\)](#) used 3D simulations to set up a wind tunnel experiment and study the exerted drag force on a stellar object that

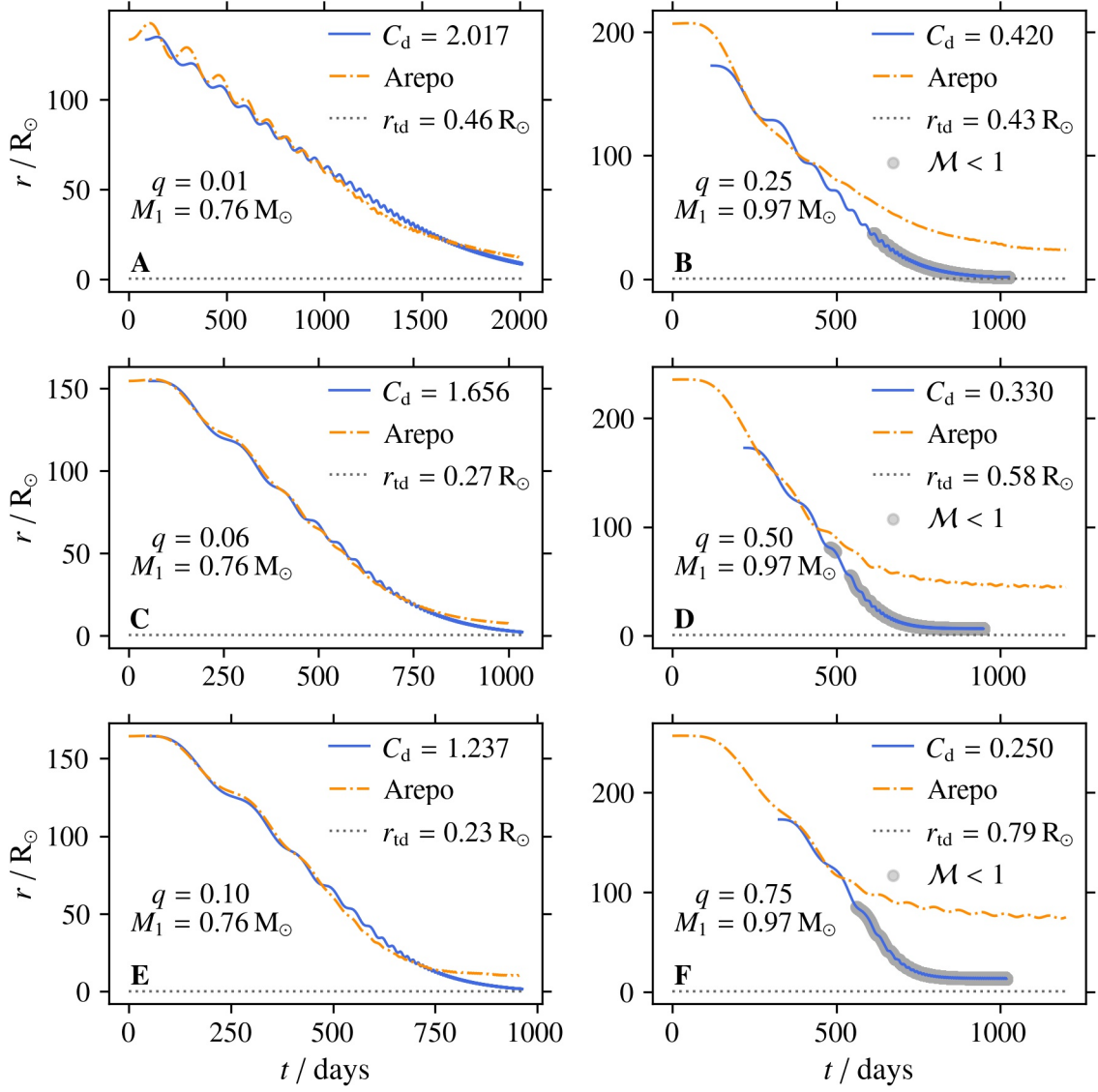


**Figure 3.5:** Separation of primary star and companion for  $q = 0.01\text{-}0.10$ ,  $M_1 = 0.76 M_\odot$  and  $q = 0.25\text{-}0.75$ ,  $M_1 = 0.97 M_\odot$  as a function of time with a drag force described by Bondi-Hoyle-Lyttleton accretion. The grey marked part is where the companion moves sub-sonically through the envelope.

moves linearly through a gas with a radial density gradient. This gas corresponds to the envelope of the primary star in our setup. With the drag forces they found in their experiment for different primary stars and companions, they then fitted drag coefficients to the formula based on Bondi-Hoyle-Lyttleton accretion (Eq. (1.4)). They then set up a fit formula which was applied in the context of this thesis. We compare how accurate it is in providing drag coefficients  $C_d$  for circular orbits around the core of a primary star, instead of linear motion. Again, the AREPO simulations are used as a comparison.

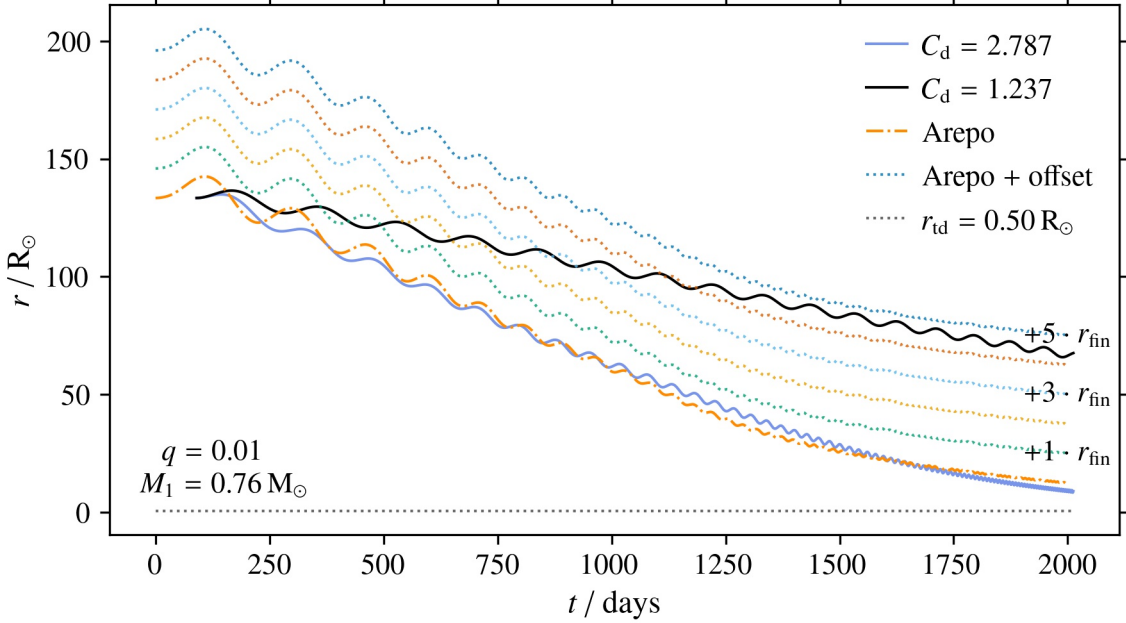


**Figure 3.6:** Separation of primary star and companion for  $q = 0.01$  as a function of time with a drag force described by Bondi-Hoyle-Lyttleton accretion. The results of AREPO are additionally plotted with an offset of  $n \cdot r_{\text{fin}}$  for  $n = 1, 2, 3, 4, 5$  in dotted lines of different colors.

We find that for  $q = 0.01$  the result of solving the equation of motion with a drag force by Bondi-Hoyle-Lyttleton accretion and a drag coefficient given by the fit formula of MacLeod & Ramirez-Ruiz (2015) shows similarity to AREPO (Figure 3.7-A). However, it is not as close to AREPO as the previously shown semi-analytic simulation with  $C_d$  fitted by minimizing  $\chi^2$  between semi-analytic and AREPO simulation (Figure 3.2). This discrepancy might be due to the fact that MacLeod & Ramirez-Ruiz (2015) only used Mach numbers of  $\mathcal{M} = 1.1, 2, 3$  but in the semi-analytic simulation the Mach number also decreases below one and does not exceed  $\mathcal{M} \approx 1.4$ . This is problematic because the parameter  $\epsilon_\rho$  (Eq. (1.6)) MacLeod & Ramirez-Ruiz (2015) defined for their fit formula becomes small for lower velocities and  $C_d$  becomes large as a consequence. This also explains why the slope of both semi-analytic simulations seem to be too steep when compared to AREPO. A higher  $C_d$  implies a higher drag force which slows down the companion causing its orbital separation to decrease faster. For  $q \geq 0.06$ , the semi-analytic approach with drag coefficients  $C_d$  provided by the fit formula of MacLeod & Ramirez-Ruiz (2015) does not lead to an in-spiral phase. This is because the companion's velocity becomes too small causing  $C_d$  to become very large ( $C_d \approx 10-40$ ). Thus, the drag force rises significantly even becoming larger than the gravitational force (Figure 3.8-B). This causes the drag force, which acts in opposite direction to the companion's motion, to stop the forward movement of the companion. Without moving on orbits around the primary, the companion is only attracted by gravity. However, the drag force

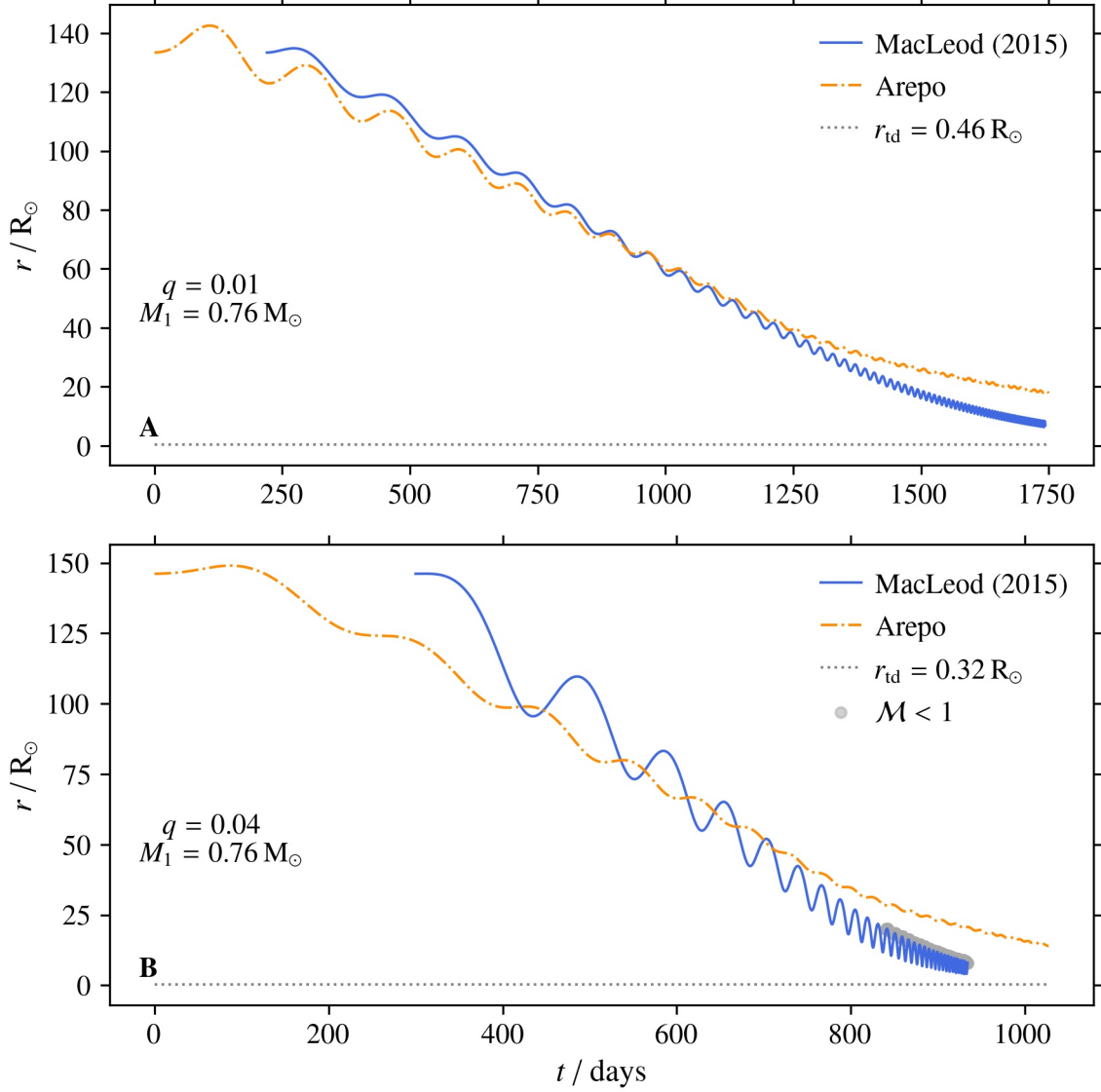


**Figure 3.7:** Separation of primary star and companion for  $q = 0.01, 0.04$  as a function of time with  $C_d$  from MacLeod & Ramirez-Ruiz (2015).

is also sufficiently large to stop the inward motion of the companion that is evoked by gravity. The companion is therefore stuck, its relative velocity in the primary's envelope is zero in any direction. This is not physical in a common envelope event. To resolve this issue, we try to use the sound speed for calculating the drag force whenever the companion reaches a sub-sonic regime, instead of using the relative velocity of the companion (i.e. the velocity of the companion compared to the gas of the envelope which rotates itself). With this we hope to be closer to the setup by MacLeod & Ramirez-Ruiz (2015) in terms of the companion's velocity. However, this measure was not enough. The visible upper limit to the drag force in Figure 3.8-B is also a consequence of this measure.

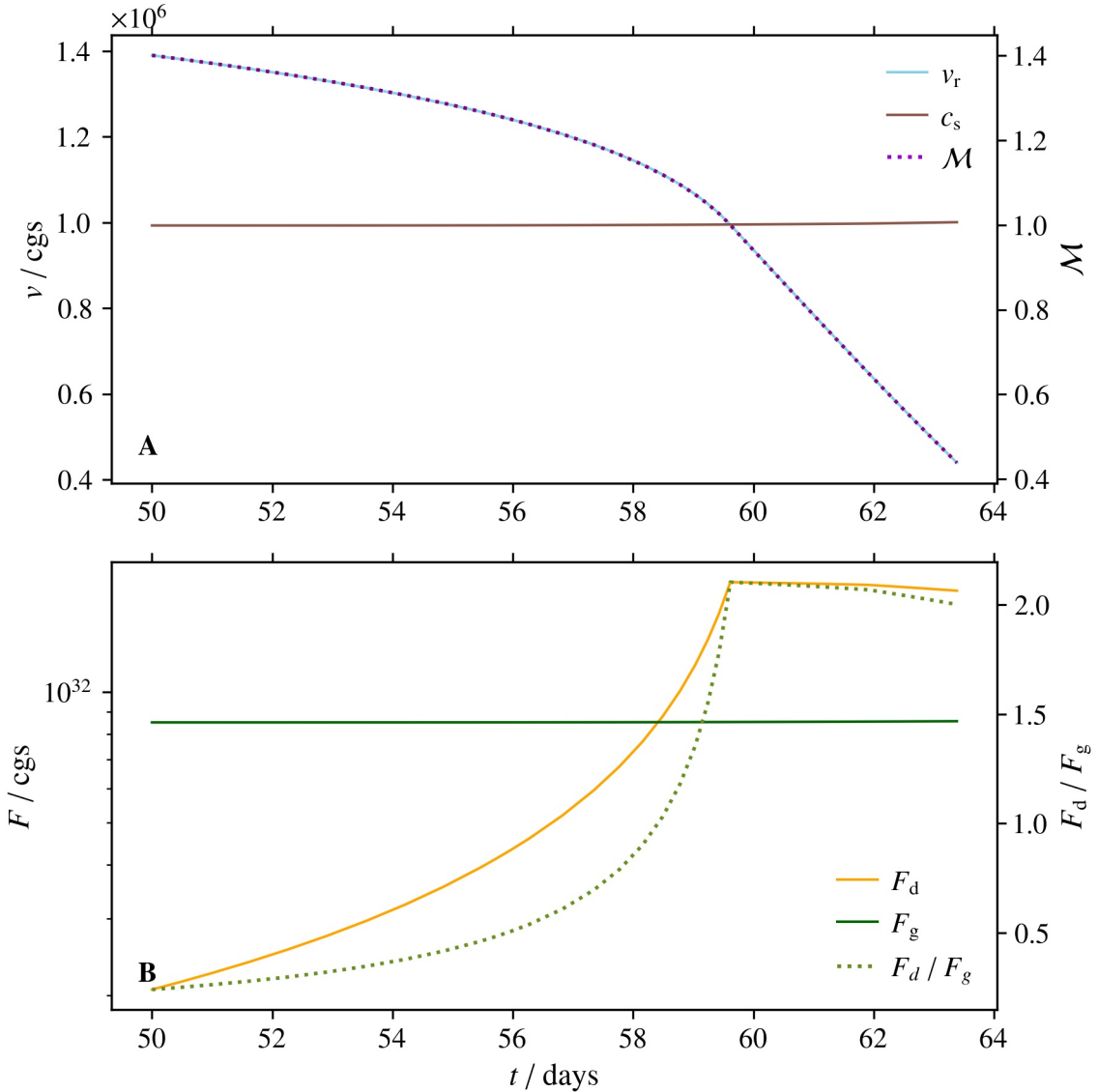


**Figure 3.8:** Velocities (A) and exerted forces (B) over time for  $q = 0.06$  with  $C_d$  from MacLeod & Ramirez-Ruiz (2015).

This leaves us to conclude that the fit formula by MacLeod & Ramirez-Ruiz (2015) is not applicable for our semi-analytic simulation. The assumption that the companion moves through the gas super-sonically with Mach numbers not smaller than  $M = 1.1$  does not hold for our setup. Even though the semi-analytic simulations do not start in a sub-sonic regime, the relative velocity of the companion is too low for the fit formula to deliver viable drag coefficients for  $q = 0.01, 0.04$ . For  $q \geq 0.06$  the provided  $C_d$  are so large that the drag force becomes significantly greater than gravity. This causes the companion to be stuck in the envelope of the primary which was explained earlier and is not physical in a common envelope event.

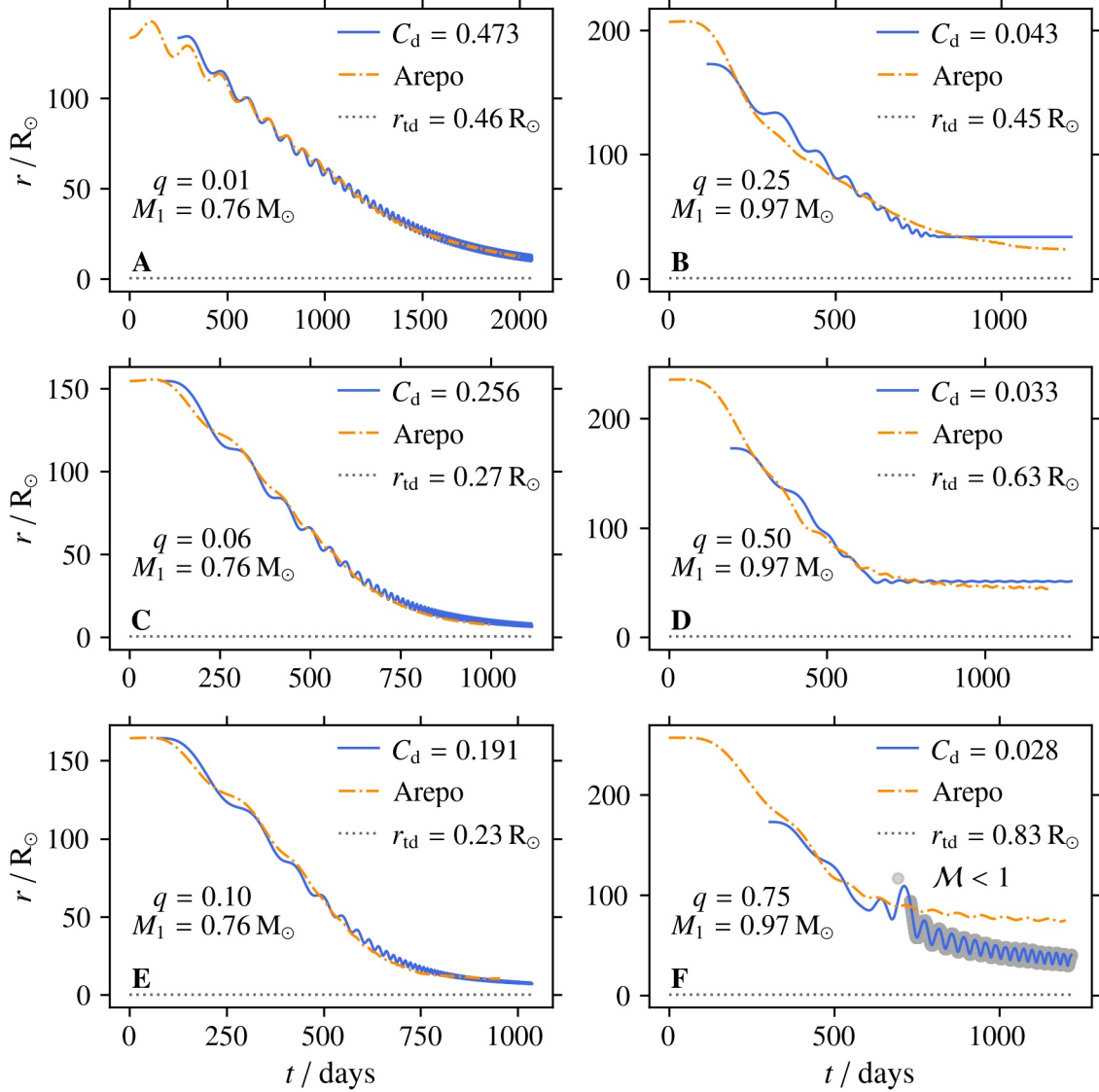


**Figure 3.9:** Separation of primary star and companion for  $q = 0.01\text{-}0.10$ ,  $M_1 = 0.76 \text{ M}_\odot$  and  $q = 0.25\text{-}0.75$ ,  $M_1 = 0.97 \text{ M}_\odot$  as a function of time with a drag force as in [Ostriker \(1999\)](#).

## 3.2 Dynamical Friction

### 3.2.1 Ostriker

With a drag force and a coulomb logarithm according to [Ostriker \(1999\)](#) (Eq. (1.10)-(1.12)) the following results are found. For  $q = 0.01\text{-}0.10$ , the semi-analytic solutions seem to be in good agreement with the results from AREPO (see Figure 3.9). The in-spiral phase and final separation are very similar and only the eccentricity differs visibly from the 3D-simulation. Eccentricity can be read from the separations plot by

looking at the oscillations of the curve. If the decrease of orbital separation happened on a perfect spiral, there would be no oscillations at all. However, since the in-spiral happens on more elliptical orbits, the separations can also become larger again, resulting in the observable oscillations. In comparison to the Bondi-Hoyle-Lyttleton formalism, these results are a lot better in terms of final separation. Here, the semi-analytic simulations seem to approach a final separation that is bigger than the tidal disruption radius and close to the one that AREPO approaches. This was not the case for the corresponding simulations in the Bondi-Hoyle-Lyttleton formalism. However, these results are visibly worse in terms of eccentricity and are more elliptical than both AREPO and also the Bondi-Hoyle-Lyttleton results.

Solving the equation of motion for  $q = 0.25-0.75$  led to numerical issues. The Coulomb logarithm defined by [Ostriker \(1999\)](#), as it is given in Eq. (1.12), is very sensitive to the choice of  $r_{\max}$  and  $r_{\min}$ . If the Mach number  $\mathcal{M}$  gets close to one, this definition for the coulomb logarithm cannot equalize the very negative first term in Eq. (1.12). This first term approaches  $-\infty$  for  $\mathcal{M} \rightarrow 1$  and thus leads to a negative drag force. This negative drag force is not physical. However, during the numerical solving of the equation of motion, it additionally causes the relative velocity  $v_{\text{rel}}$  of the companion to rise which then again increases the Mach number  $\mathcal{M}$ . With higher  $\mathcal{M}$ , the Coulomb logarithm becomes larger than the first, always negative term in Eq. (1.12) and therefore the drag force can become positive again which will lead to a decrease in  $v_{\text{rel}}$ . This will cause  $\mathcal{M}$  to approach one again which results in a negative drag force. A cycle of rising and falling  $\mathcal{M}$  is created and if these steps are small enough, the Mach number  $\mathcal{M}$  will never become smaller than one, always 'bouncing' back and forth close to one but always greater. This, then, also leads to a stable final separation which is more an artifact of this issue than it is physical. Nevertheless, it is interesting to note that the final separations are close to the ones from AREPO. Additionally, the point where the 'bouncing' starts, i.e. the point where in theory a sub-sonic regime should start, coincides with the point where the AREPO results start to approach a stable final separation.

For  $q = 0.75$  the change in Mach number at  $t \approx 730$  days is large enough as  $\mathcal{M}$  suddenly drops below one far enough so that the coulomb logarithm can equalize the negative term and the drag force can become positive. This breaks the 'bouncing' cycle and the companion can change to a sub-sonic regime. However, Figure 3.9 shows that the result is not in line with AREPO in terms of final separation and eccentricity. Especially when the sub-sonic regime is reached, eccentricity and orbital separation differ significantly from the AREPO simulation. Nevertheless, this simulation seems to approach a final separation larger than the tidal disruption radius just like in AREPO. Figure 3.10 shows the explained mechanisms behind the 'bouncing' which takes place from around day 600 up until around day 730. It then ends in a sudden increase of the drag force that pushes the companion into a sub-sonic regime. During the bouncing we can see how the drag force becomes negative multiple times always causing an increase in the companion's orbital separation which then again leads to a decrease in  $v_{\text{rel}}$  and  $c_s$ . Because these two components change at different rates, the Mach number can become larger moving away from one so that the drag

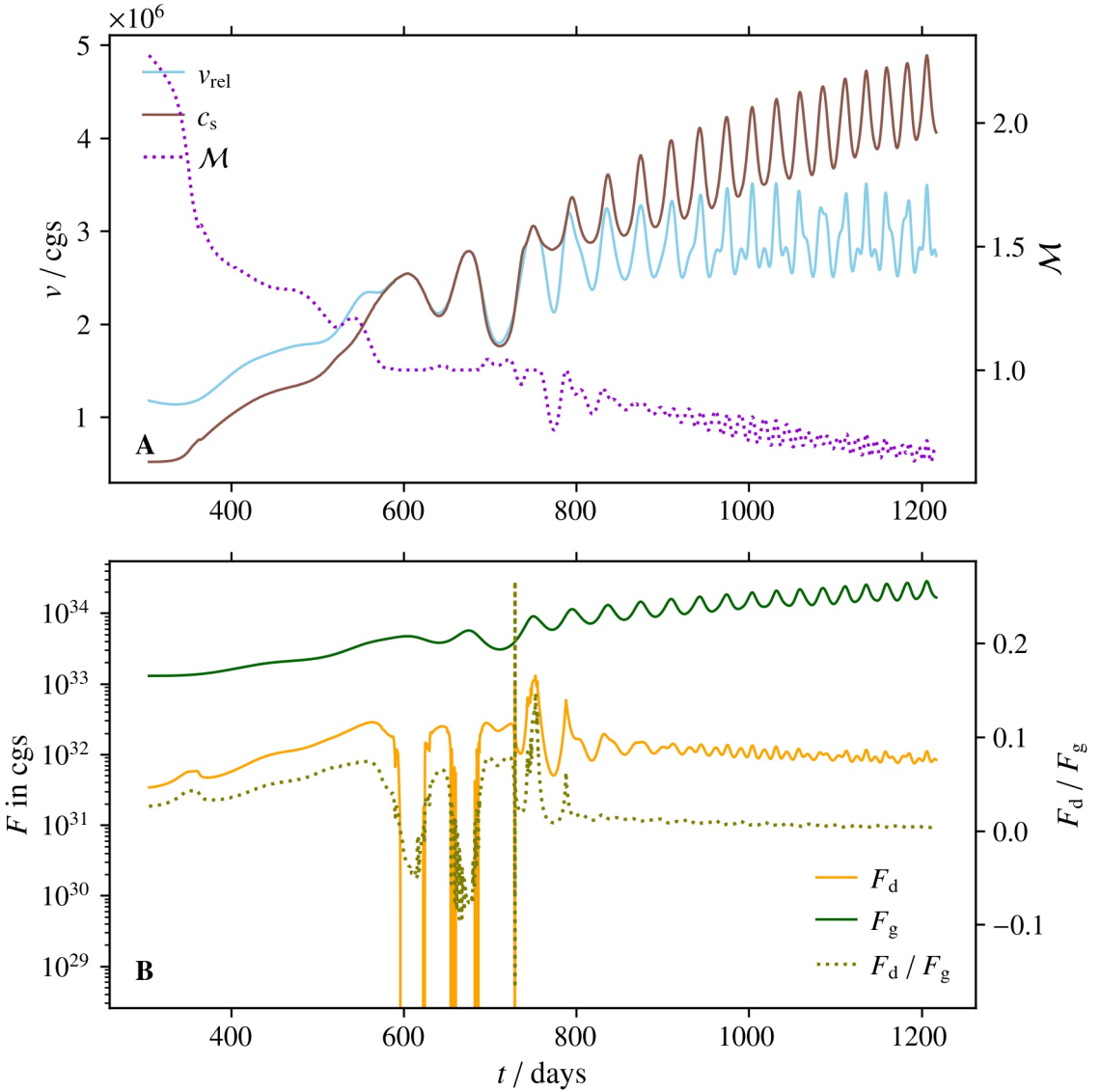


**Figure 3.10:** Velocities (A) and exerted forces (B) over time for  $q = 0.75$  with a drag force as in Ostriker (1999).

force can become positive again. Note that the scale for the forces in Figure 3.10 is logarithmic which means that negative values cannot be displayed. However, the ratio  $F_d/F_g$  becomes negative and thus indicates that  $F_d$  must also be negative.

Also in terms of change in  $C_d$ , the formalism from Ostriker (1999) seems to be superior to Bondi-Hoyle-Lyttleton accretion and scales more correctly with  $q$ . As before, the semi-analytic simulation for  $q = 0.01$ , but with the  $C_d$  that was found for  $q = 0.10$ , was plotted to compare it to the semi-analytic simulation for  $q = 0.01$  with its best fitting  $C_d$  (Figure 3.11). We find that  $\Delta r \approx 4 \cdot r_{\text{fin}}$ , which is slightly less than it was for Bondi-Hoyle-Lyttleton accretion. This indicates that the drag force from Ostriker (1999) indeed scales better with the mass ratio of companion

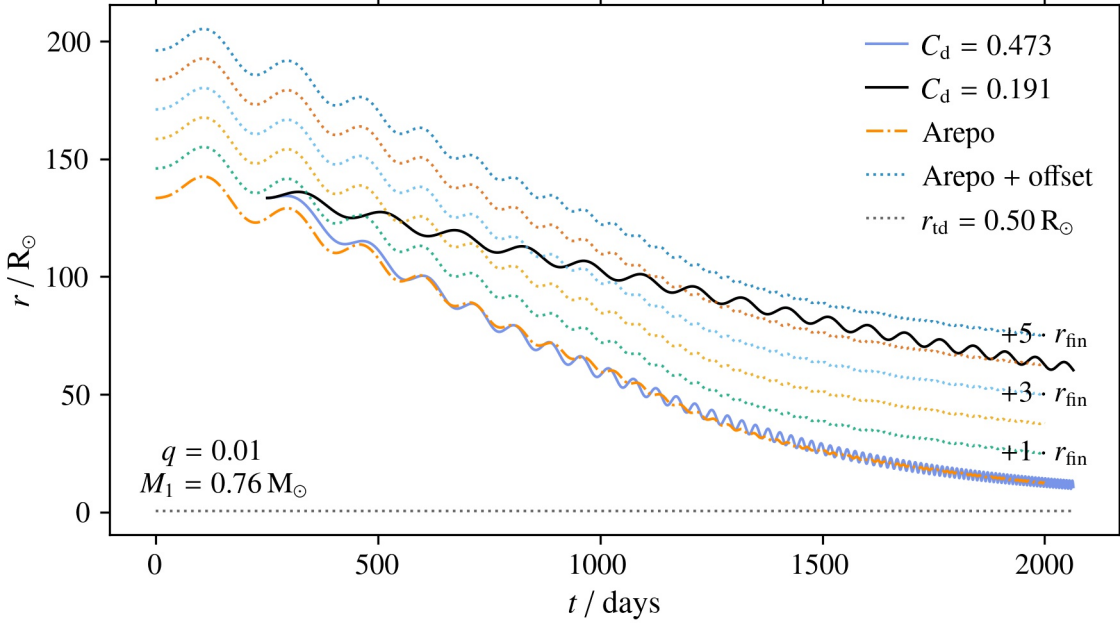


**Figure 3.11:** Separation of primary star and companion for  $q = 0.01$  as a function of time with a drag force as in Ostriker (1999). The results of AREPO are additionally plotted with an offset of  $n \cdot r_{\text{fin}}$  for  $n = 1, 2, 3, 4, 5$  in dotted lines of different colors.

and primary star even if only slightly.

Therefore, we can conclude that the drag force and coulomb logarithm as in Ostriker (1999) seem to be more likely to reach a final separation of companion and primary. Additionally, they seem to scale better with the companion's mass than the formalism based on Bondi-Hoyle-Lyttleton accretion. However, this formalism leads to more elliptical orbits which is less similar to AREPO and also causes issues for mass ratios  $f q \geq 0.25$ . These issues stem from the sensitivity to  $r_{\max}$  and  $r_{\min}$  and could maybe be resolved by introducing numerical methods such as changing  $r_{\min}$  at one or more points during the simulation. Others (e.g. Kim & Kim, 2007) tried to define the coulomb logarithm differently, thereby eliminating the 'bouncing' as we will see in the next section. A summary of the determined drag coefficients for all formalisms can be found in Table 3.1.

### 3.2.2 Kim and Kim

With the refinement of dynamical friction for a perturber on circular orbits in a gaseous medium from Kim & Kim (2007), the results of our semi-analytic simulation get even more comparable to the 3D AREPO simulation. Figure 3.12 shows that for  $q = 0.01-0.10$  the general course of the separation over time seems to be in good agreement with the AREPO result. Also in terms of final separation, they seem to be well in line with each other as they all approach a final separation greater than the tidal disruption radius. However, the eccentricities deviate again. While the orbits

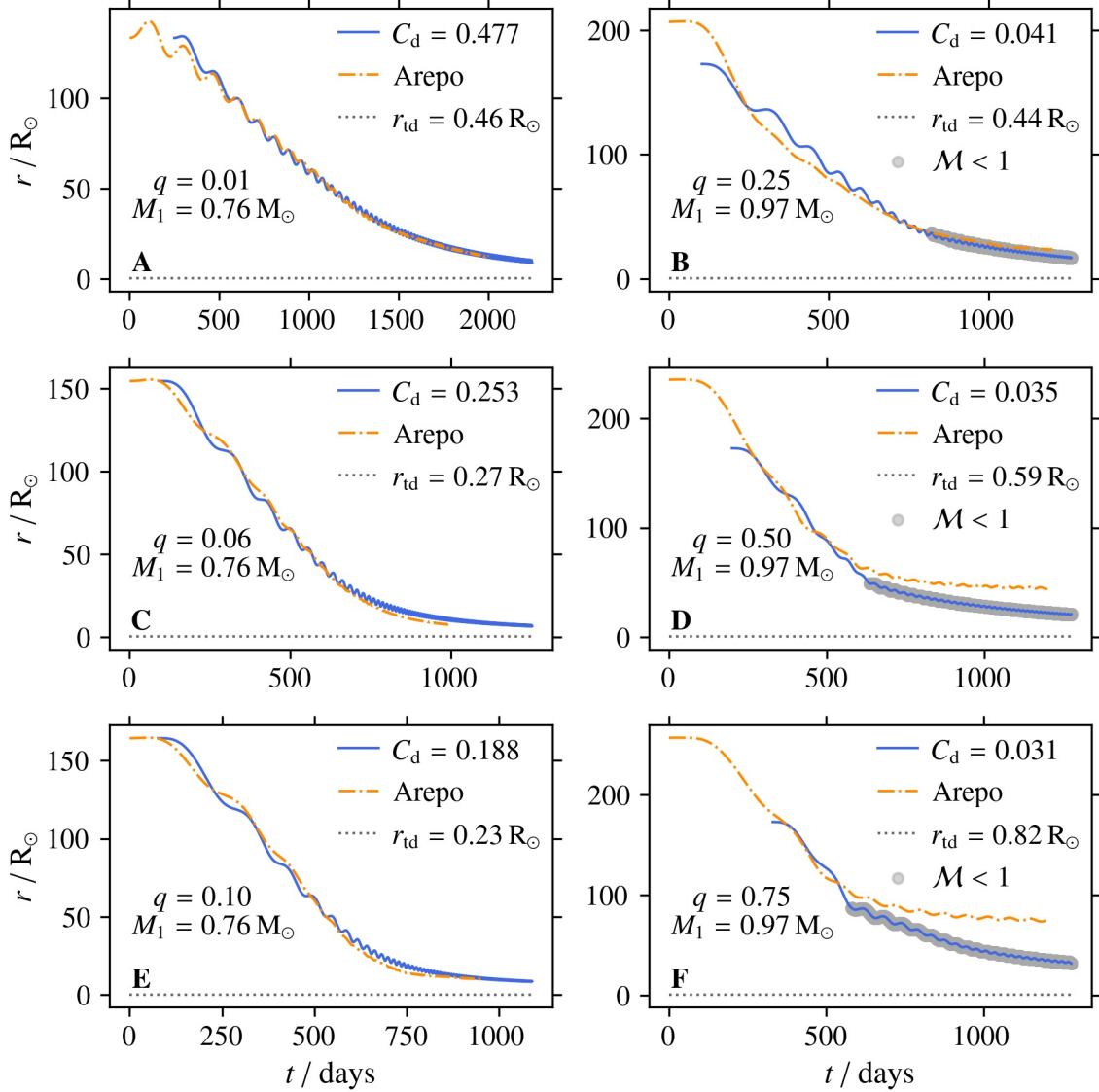


**Figure 3.12:** Separation of primary star and companion for  $q = 0.01\text{-}0.10$ ,  $M_1 = 0.76 M_\odot$  and  $q = 0.25\text{-}0.75$ ,  $M_1 = 0.97 M_\odot$  as a function of time with a drag force as in [Kim & Kim \(2007\)](#).

in the different AREPO simulations seem to get more circular as they approach a final separation, they stay slightly elliptical in the semi-analytic simulations which can be seen by the oscillations of the separation curve.

Even for  $q = 0.25\text{-}0.75$  the formalism of [Kim & Kim \(2007\)](#) seems to be a lot better suited than the two previously discussed formalisms. For  $q = 0.25$  the similarity to the AREPO simulation is remarkable and significantly better than the Bondi-Hoyle-Lyttleton and [Ostriker \(1999\)](#) formalisms. Increasing  $q$  from there on leads to significant deviations from AREPO again. Although, for both  $q = 0.50$  and  $q = 0.75$  the semi-analytic simulations approach a final separation larger than the tidal

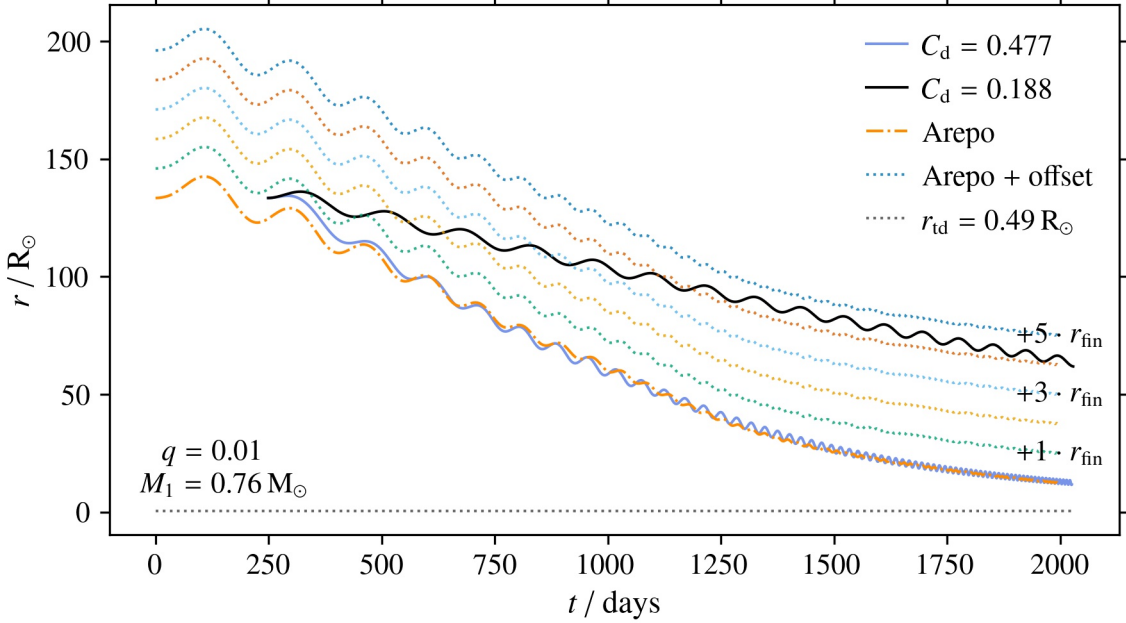


**Figure 3.13:** Separation of primary star and companion for  $q = 0.01$  as a function of time with a drag force as in Kim & Kim (2007). The results of AREPO are additionally plotted with an offset of  $n \cdot r_{\text{fin}}$  for  $n = 1, 2, 3, 4, 5$  in dotted lines of different colors.

disruption radius, they are different than those found with AREPO. It is also to note that for those  $q$ , the transition from super-sonic to sub-sonic regime seems to be less smooth than it was for previous simulations (e.g. Bondi-Hoyle-Lyttleton). Here, a visible change in the course of the separation is introduced. These deviations are likely to stem from the assumption that the density of the primary's envelope is constant over the course of the common envelope phase. This assumption has been in place for this and all the previous formalisms but will change with the next one.

In terms of change in  $C_d$  for different  $q$ , this formalism by Kim & Kim (2007) is similarly good as the formalism by Ostriker (1999) with a difference in final separations of  $\Delta r \geq 4 \cdot r_{\text{fin}}$ . The similarity of Ostriker (1999) and Kim & Kim (2007) for low mass ratios, where the Mach number does not come close to one, is not surprising and was already mentioned in the introduction (see Figure 1.1). Again, for  $q \geq 0.25$  a comparison like this is inconclusive because it indicates how good the current formalism is compared to another formalism that delivers reasonable results. Since none of the previous formalisms was able to recreate the course of the in-spiral phase for  $q \geq 0.25$ , it is not necessary to compare the change in  $C_d$  for these mass ratios. A summary of the determined drag coefficients for all formalisms can be found in Table 3.1.

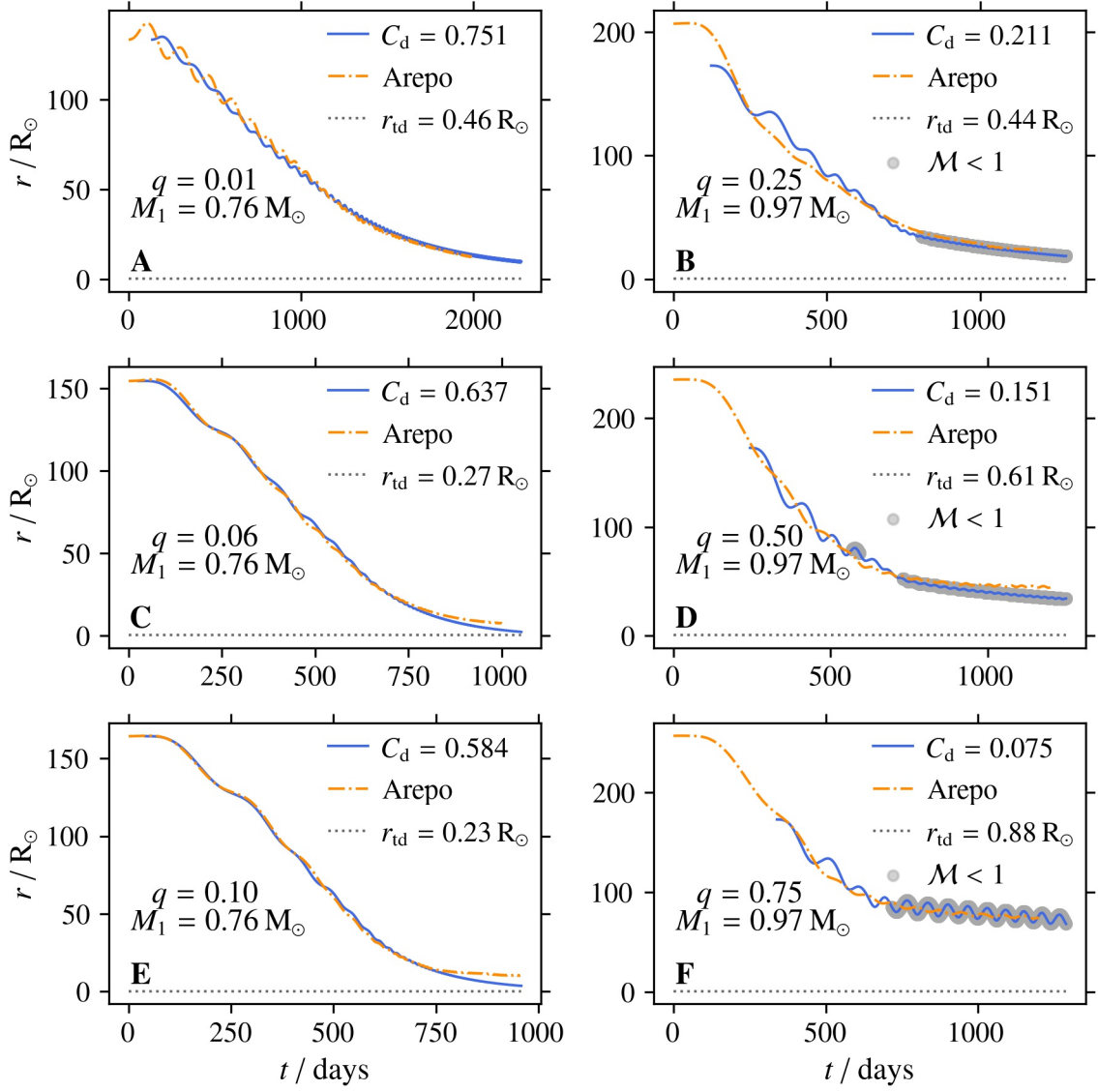


**Figure 3.14:** Separation of primary star and companion for  $q = 0.01\text{-}0.10$ ,  $M_1 = 0.76 M_\odot$  and  $q = 0.25\text{-}0.75$ ,  $M_1 = 0.97 M_\odot$  as a function of time with a drag force as in [Kim \(2010\)](#).

### 3.2.3 Kim

After further refining their work from 2007 for nonlinear dynamical friction, [Kim \(2010\)](#) introduced another formula for the drag force and the coulomb logarithm. For the first time in this thesis, also taking into account that the density of the primary's envelope changes as a response to the companion moving through it. With this formalism, the in-spiral phase could be simulated with unprecedented similarity to AREPO. Especially for  $q = 0.06$  and  $q = 0.10$ , there is almost no difference between semi-analytic and AREPO simulation (see Figure 3.14-C, -E) and only towards the

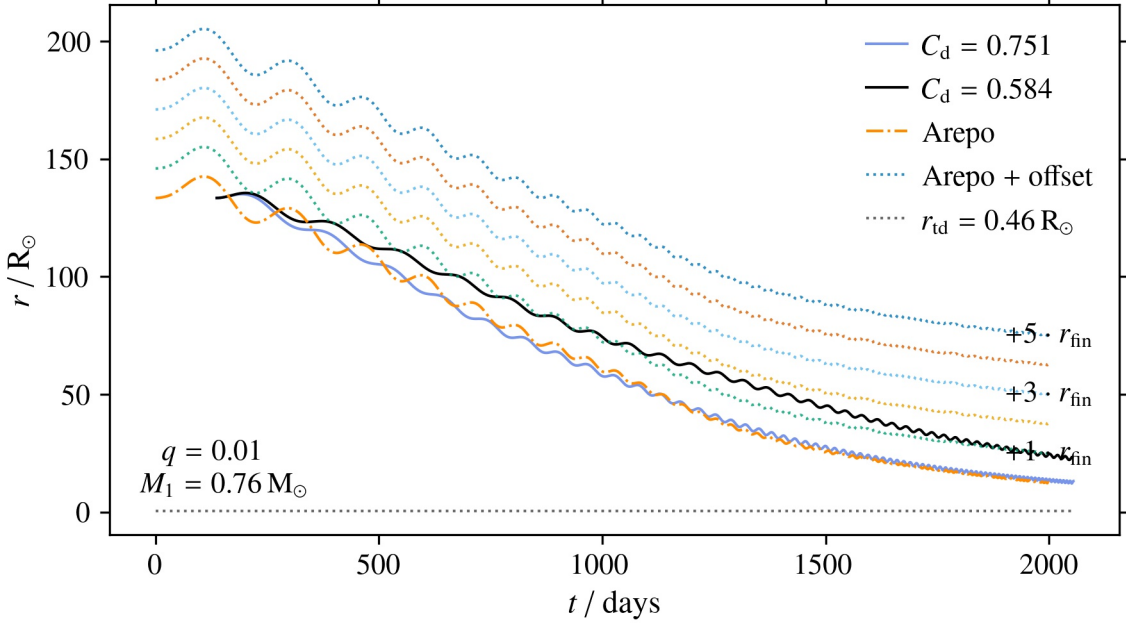


**Figure 3.15:** Separation of primary star and companion for  $q = 0.01$  as a function of time with a drag force as in Kim (2010). The results of AREPO are additionally plotted with an offset of  $n \cdot r_{\text{fin}}$  for  $n = 1, 2, 3, 4, 5$  in dotted lines of different colors.

end of the simulations the semi-analytic model starts to deviate from AREPO. For these two mass ratios (maybe also for  $q = 0.01$ ), primary and companion do not approach a final separation greater than the tidal disruption radius. Instead, they approach separations where the companion would get ripped apart by the tidal forces exerted by the primary's mass. The objects would be considered to merge. This was not the case with the previous formalism (Kim & Kim, 2007), however, there eccentricity was not as similar to AREPO as with this formalism.

For  $q \geq 0.25$  this is also the formalism that works the best. Although the eccentricities of the semi-analytic simulations are different than those of AREPO it is remarkable that the drag force of Kim (2010) is able to capture the in-spiral phase with such similarity to the 3D simulation. Even the final separations are in line with those reached by AREPO. Unlike for  $q = 0.06$  and  $q = 0.10$ , the final separations for  $q \geq 0.25$  seem to stay larger than the tidal disruption radius over a long period of time.

Also when looking at the change of  $C_d$  for  $q = 0.01-0.10$ , this formalism is outstanding. Using the drag coefficient that was originally found for  $q = 0.10$ , the semi-analytic simulation for  $q = 0.01$  only differs slightly from the simulation with the best fitting  $C_d$ . The difference in final separation which previously was at  $\Delta r \approx 4$ , is now at only  $\Delta r \approx 1$ . This means that this formalism by Kim (2010) scales better with the companion's mass than all the previous formalisms. However, this is also the only formalism that takes a change of the envelope's density into account. We would therefore expect the drag coefficients  $C_d$  to change less with mass ratio than

previous formalisms. This is because the change in density is in parts taken into account by the drag force itself and does not have to be fully compensated by  $C_d$ . A summary of the determined drag coefficients for all formalisms can be found in Table 3.1.

**Table 3.1:** Determined  $C_d$  for different  $q$  with drag forces from all discussed formalisms. BHL: Bondi-Hoyle-Lyttleton; O99: [Ostriker \(1999\)](#); KK07: [Kim & Kim \(2007\)](#); K10: [Kim \(2010\)](#)

$q$	$M_1 = 0.76 \text{ M}_\odot$				$M_1 = 0.97 \text{ M}_\odot$			
	0.01	0.04	0.06	0.10	0.25	0.50	0.75	
$C_d$	BHL	2.787	2.017	1.656	1.237	0.42	0.33	0.25
	O99	0.473	0.301	0.256	0.191	0.043	0.033	0.028
	KK07	0.477	0.302	0.253	0.188	0.041	0.035	0.031
	K10	0.751	0.620	0.637	0.584	0.211	0.151	0.075

### 3.3 Role of Initial Co-Rotation

Currently, the choice of the co-rotation factor in common envelope simulations is somewhat arbitrary. Different research groups working in that field have different preferences and choices. This section will try to shed some light on the actual importance and consequences of choosing the initial co-rotation factor  $f_{\text{corot}}$ .

Using the drag formalism of [Kim & Kim \(2007\)](#) because it has the best accuracy in resolving the final separation (which will be discussed in further detail in the next section) and simply plugging in a range of different initial co-rotation factors  $f_{\text{corot}}$ , we find the result in Figure 3.16. It shows the known separation-over-time plot with the AREPO result and also four semi-analytic simulations with different  $f_{\text{corot}}$ . From the different colors it is immediately visible that for decreasing  $f_{\text{corot}}$  the timescale on which the in-spiral phase takes place increases. The final separation itself seems to stay the same for all tested  $f_{\text{corot}}$ .

The fact that the timescale of the in-spiral phase increases for lower  $f_{\text{corot}}$  may seem counter-intuitive at first. This is because one may think that a lower  $f_{\text{corot}}$  means a higher relative velocity  $v_{\text{rel}}$  - which it does - that then should result in a higher drag force and therefore in a faster in-spiral phase - which it does not. In order to understand this, the Mach number  $\mathcal{M}$  was plotted over the separation of companion and primary star for different  $f_{\text{corot}}$  in Figure 3.17. In these plots the Mach number has been calculated by determining the orbital velocity for circular Kepler orbits for a wide range of radii and dividing by the sound speed at the specific radii in the envelope. The sound speed is taken from the MESA profile of the primary star. One can see that near the surface of the primary the Mach number increases significantly for decreasing  $f_{\text{corot}}$ . Near the core of the primary, the Mach number almost does not change at all for different  $f_{\text{corot}}$ . This can be explained by looking at the formulas

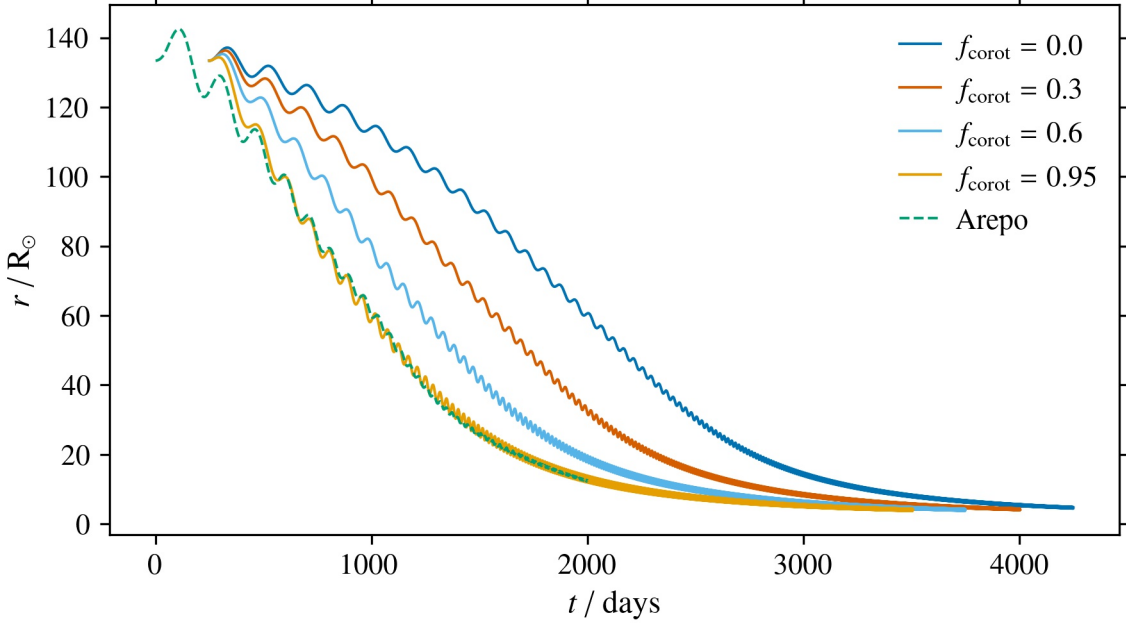


**Figure 3.16:** Separation of primary star and companion for  $q = 0.01$  as a function of time with a drag force as in [Kim & Kim \(2007\)](#) for different initial co-rotation.

for the orbital velocity of the companion and the angular speed of the envelope. The orbital speed is  $v_{\text{orb}} = \sqrt{GM_1/r}$ , thus increases for decreasing orbital separation. The angular velocity of the envelope, which was assumed to be a solid body rotator (i.e. constant angular velocity at all radii), is  $v_{\text{env}} = \omega \cdot r$  meaning it decreases linearly with decreasing orbital separation. For the semi-analytic models of different  $f_{\text{corot}}$ , the Mach number is calculated with the relative velocity  $v_{\text{rel}} = v_{\text{orb}} - v_{\text{env}}$ . We know, for decreasing orbital separations  $v_{\text{env}}$  becomes small compared to  $v_{\text{orb}}$ . Thus,  $v_{\text{rel}} \approx v_{\text{orb}}$  is valid for small orbital separations. Since  $f_{\text{corot}}$  only changes  $v_{\text{env}}$  and has no influence on  $v_{\text{orb}}$ ,  $v_{\text{rel}}$  and therefore also the Mach number are not changed significantly for small orbital separations when using different  $f_{\text{corot}}$ . This is exactly what can be observed in Figure 3.17. Consequentially, the curves in Figure 3.16 differ significantly in the beginning but then start approaching each other again. For comparison and confirmation Figure 3.17 also includes the curve of a semi-analytic simulation with the corresponding mass ratio and  $f_{\text{corot}} = 0.95$  which is how the AREPO simulation was set up. The general course seems to be in good agreement taking into consideration that the companion is not on circular orbits in the simulation as it was assumed for the curves of different  $f_{\text{corot}}$ . Additionally, the relative velocity is significantly lower in the simulations due to the continued deceleration by the drag force. Having confirmed that the Mach number rises with decreasing  $f_{\text{corot}}$ , Figure 1.1 now explains why the timescale of the in-spiral phase increases. There, we can see that a drag force described by dynamical friction as in [Ostriker \(1999\)](#) and [Kim & Kim \(2007\)](#) has a peak at a Mach number of slightly over one but then decreases with increasing Mach number.

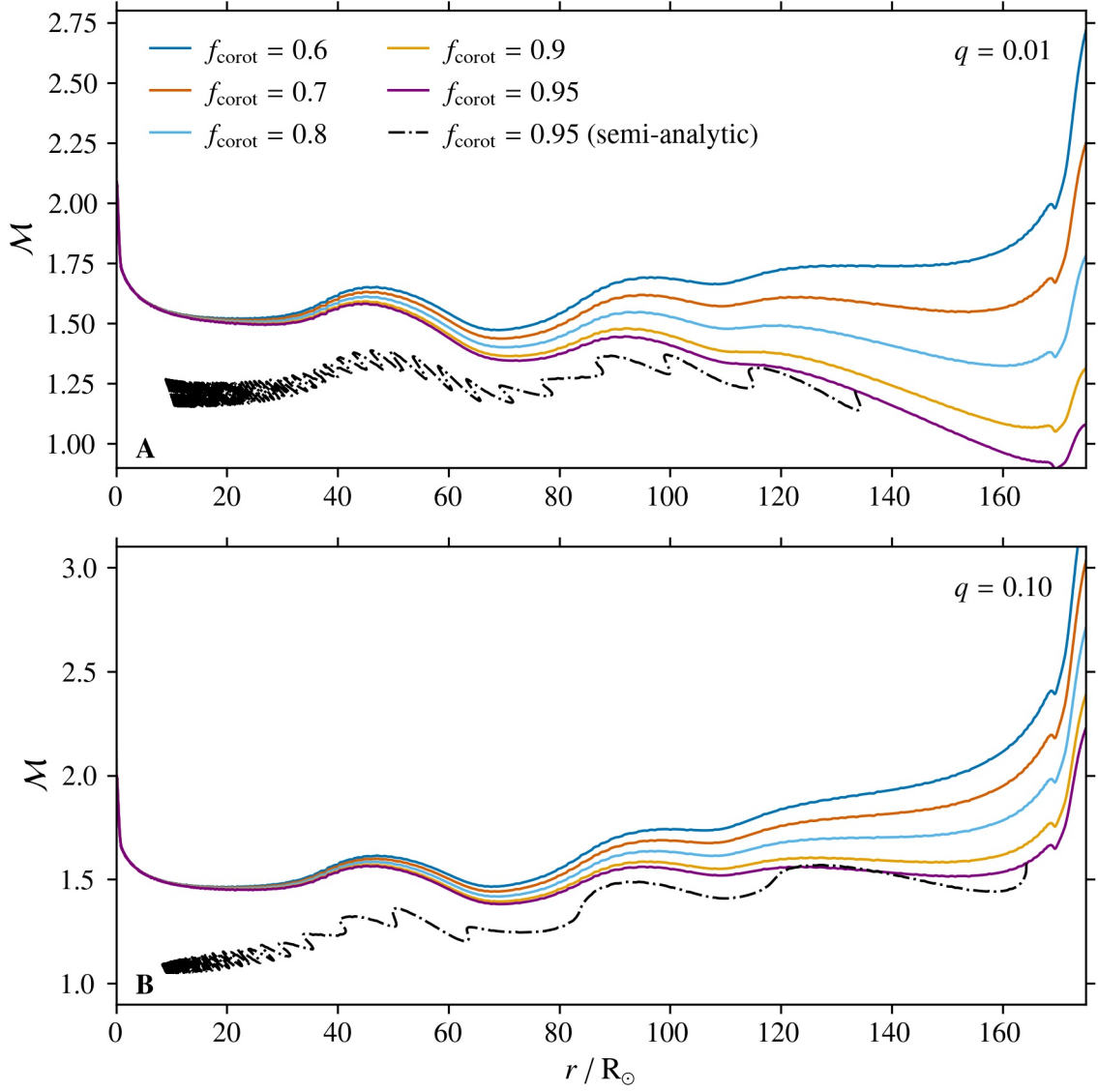


**Figure 3.17:** Mach number as a function of orbital separation of primary star and companion for different initial co-rotation.

### 3.4 Final Separation

Throughout this work, it has become clear that the end of the in-spiral phase and the approaching of a final separation is an intrinsic feature of a common envelope phase and also part of a simplistic semi-analytic simulation. This section will go over the insights that can be gained from the results previously discussed about said feature and try to explain the mechanisms behind it.

In all of the shown separation-over-time plots a slowing-down of the in-spiral is visible. Some of them approach separations where tidal forces would rip the companion apart before it could advance further into the primary's envelope and the

two objects would merge (e.g. Figure 3.5-E). But others actually seem to approach a constant final separation (e.g. Figure 3.14-C). One feature all of them have in common is that towards the end of the in-spiral phase the ratio  $F_d / F_g$  approaches zero (e.g. Figure 3.4). This means that the gravitational force is bigger than the drag force by orders of magnitude. If this is the case, the exerted drag changes the overall motion of the companion only by a negligible fraction compared to gravity. The proportion of the gravitational force on the total change of the companion's velocity is then significantly bigger than that of the drag force.

As it can be seen in any forces plot (e.g. Figure A.1, Figure A.3, Figure A.5),  $F_g$  increases with decreasing separation. This can be explained by looking at the formula  $F_g \propto M_1/r^2$ , where  $M_1$  is the mass of the primary enclosed within the companion's separation around the primary's core and  $r$  is the orbital separation. For decreasing  $r$ ,  $M_1$  decreases slower than  $r^2$  and thus  $F_g$  increases with decreasing orbital separation.

The behavior of  $F_d$  is more complex since it depends on several correlated parameters like  $\rho$  and  $v_{\text{rel}}$  which both depend on  $r$  and  $\mathcal{M}$ , which directly depends on  $v_{\text{rel}}$  but also indirectly on  $\rho$  because of  $c_s$ . However, we can approximately say that the course of the Mach number  $\mathcal{M}$  is a good indicator of the course of the drag force.

To explain what drives the drag force, we will look into the two components of  $\mathcal{M} = v_{\text{rel}}/c_s$  in more detail. The sound speed  $c_s$  depends on the density of the envelope which increases with decreasing orbital separations since temperatures are much higher close to the stellar core than near the surface. Therefore,  $c_s$  increases for decreasing separations too. And, as it was discussed in the previous section on co-rotation, the relative velocity  $v_{\text{rel}}$  increases with decreasing separations as well. Since both of these quantities increase for decreasing orbital separations, the course of the Mach number  $\mathcal{M}$  cannot be generalized. All we can say is that if  $c_s$  increases faster than  $v_{\text{rel}}$ , the Mach number will decrease and vice versa.

If  $\mathcal{M}$  approaches one from below or above, the drag force increases (see Figure 1.1) and otherwise it decreases. Even if  $\mathcal{M}$  stays roughly constant, as long as  $r$  still decreases, it causes  $v_{\text{rel}}$  to rise and while  $\rho$  also rises with decreasing  $r$  it does not rise fast enough to counteract the proportionality of  $F_d$  to  $1/v_{\text{rel}}^2$  (see Eq. (1.10)). Hence, the drag force would also decrease if  $\mathcal{M}$  was constant for some time. In the beginning of the in-spiral phase,  $c_s$  is smaller than  $v_{\text{rel}}$  but catches up quickly, decreasing the Mach number towards one and therefore increasing the drag force. At some point both components approach the same value or in cases of higher mass ratios,  $c_s$  becomes bigger than  $v_{\text{rel}}$  entering a sub-sonic regime ( $\mathcal{M} < 1$ ). Both options, staying at a Mach number that is roughly constant or decreasing in a subsonic regime, cause the drag force to either stay approximately constant, too, or to decrease.

In any case, from some point on  $F_d$  will increase slower than  $F_g$  (if at all) and thus  $F_d/F_g$  will approach zero from then on. The companion's in-spiral will then slow down as the proportion of the drag force on the total change of the companion's motion shrinks compared to the proportion of gravity.

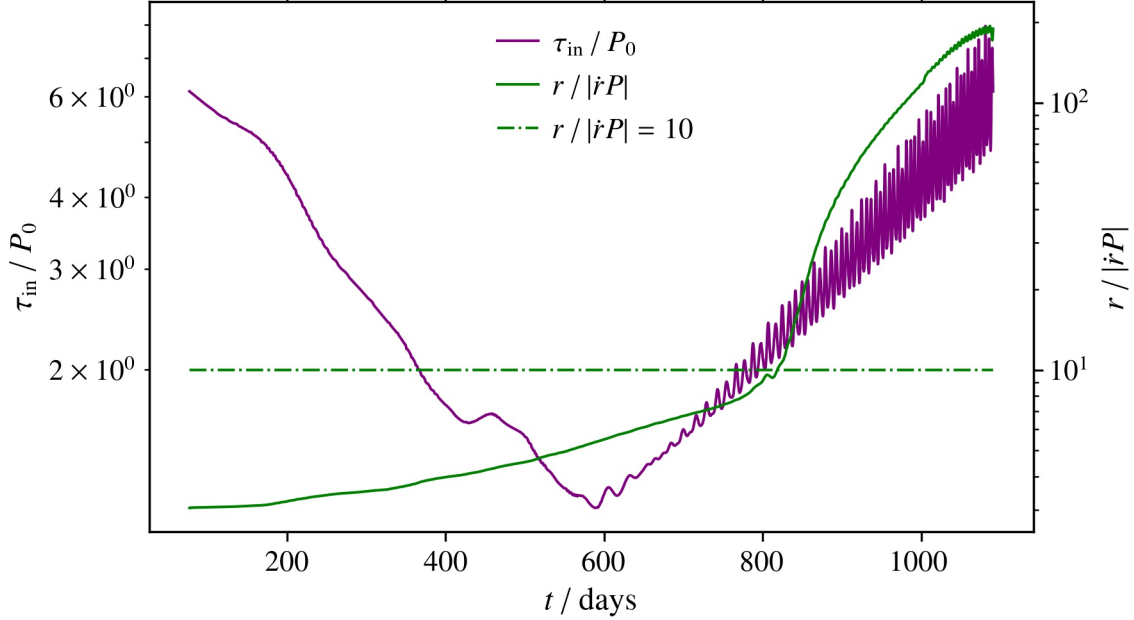


**Figure 3.18:** Angular momentum timescale in purple and orbital separation timescale in green. The limit which indicates the end of the in-spiral (Ivanova & Nandez, 2016) is plotted as green dashed-dotted line.

To pin-point the end of the in-spiral phase and to answer whether the companion reaches a stable final separation or not, different criteria than  $F_d/F_g$  approaching zero are required. For this matter the timescales defined in Equation 2.24 and Equation 2.30 are used.

$\tau_{in}/P_0$  expresses how long it would take to remove all of the angular momentum from the companion with the current drag force in units of the initial orbital period. In other words, how many full initial orbits the companion could complete while subjected to the current drag force until it would stop orbiting the primary star. Since the in-spiral speeds up in the beginning and the drag force increases,  $\tau_{in}/P_0$  decreases (see Figure 3.18 or appendix). This is because it would take a shorter amount of time to fully remove the angular momentum from the companion with the current drag force.  $\tau_{in}/P_0$  then reaches a minimum when  $F_d$  starts to increase more slowly or even starts to decrease. This marks the turning point of the in-spiral phase where it transitions from speeding-up to slowing-down.

$r/|\dot{r}P|$  expresses how long it would take to fully remove the orbital separation between primary and companion in units of the current orbital period. In other words, how many full orbits could the companion complete before it would reach the primary's core, if the orbital separation keeps decreasing at the current rate. In our simulations, this timescale only increases over time (see Figure 3.18 or appendix) since the orbital period  $P$  decreases faster than the time  $r/|\dot{r}|$  it would take to fully remove the orbital separation. Overall, this means that  $r/|\dot{r}P|$  increases over time.  $r/|\dot{r}P|$  then reaches a point where its slope suddenly increases significantly. This

corresponds to the point of time where the orbital separation between primary star and companion stops decreasing rapidly and approaches an approximately constant final separation. Therefore, this may be a good definition for the end of the in-spiral phase.

Looking at the timescale plots for all the simulations (e.g. Figure A.2, Figure A.4, Figure A.6), it seems that if the companion approaches a final separation,  $\tau_{\text{in}}/P_0$  also shows a minimum at an earlier point. If the in-spiral slows down but does not approach a final separation,  $\tau_{\text{in}}/P_0$  does not show a minimum. This is plausible because if  $\tau_{\text{in}}/P_0$  does not show a minimum, it means that the drag force did not start to rise less steep or stop increasing entirely. Thus, the companion did not stop advancing deeper into the envelope of the primary. However, in some cases (BH,  $q=0.25$ ),  $\tau_{\text{in}}/P_0$  shows the minimum so late that the companion is already too close to the primary to reach a final separation before being ripped apart by tidal forces. After all, the minimum of  $\tau_{\text{in}}/P_0$  only indicates the turning point from speeding-up to slowing-down the in-spiral and not the the end of it.

To characterize the end of the in-spiral phase,  $r/|\dot{r}P|$  seems to be better suited. In their paper [Ivanova & Nandez \(2016\)](#) empirically defined the in-spiral to have ended when the change of orbital separation reaches  $r/|\dot{r}P| \gtrsim 10$ . This is a good approximation for most of our simulations as it almost always crosses  $r/|\dot{r}P|$  at the point where the slope suddenly increases significantly which we said could be a good definition for the end of the in-spiral phase earlier. It is important to note that here  $\dot{r}$  was determined by taking the difference of  $r$  (and  $t$ ) at one timestep and  $r$  (and  $t$ ) at the next timestep. Because of the way the used numerical solver works, the timesteps vary in size and can also be negative. This leads to a lot of noise in  $\dot{r}$  which we tried to resolve by applying a 1D uniform filter and averaging over neighboring elements. With those two methods we found the results that were shown and discussed above.

In conclusion, it seems that  $r/|\dot{r}P|$  may be well suited for finding the end of the in-spiral phase at an change of orbital separation  $r/|\dot{r}P| \approx 10$  but not for determining if the simulation reaches a stable final separation. This is because it did not show an obvious change in behavior for simulations that reach a stable separation or those that do not. For this matter  $\tau_{\text{in}}/P_0$  seems to be the better choice. If  $\tau_{\text{in}}/P_0$  shows a minimum and if the companion is not already too close to the primary, chances are high that the companion will soon reach a final orbital separation.

## 4 Discussion

The results suggest that it is indeed possible to match the evolution of the orbital separation in a common envelope phase with a semi-analytic model. This is an important insight because it greatly reduces the computation time needed to obtain a simulated in-spiral phase with good accuracy. However, none of the applied formalisms could be calibrated for a constant drag coefficient. This means that for other mass ratios or primary stars with a different internal structure than the ones used in this thesis, the drag coefficient  $C_d$  would have to be guessed accordingly. This could be done by interpolating the found  $C_d$ . Of course, it could also be calibrated to a corresponding AREPO simulation but this would not safe any time since the AREPO simulation would have to be carried out first.

### 4.1 Assumption of Constant Density

For all of our semi-analytic simulations, two static MESA profiles have been used. This means that the density of the primary's envelope does not change over the course of the common envelope phase. By this, we assume that the companion does not influence the structure of the envelope by moving through it. This assumption is false. Although it is not yet fully understood how much the companion disturbs the envelope, it is known that more massive companions lead to more significant changes in the envelope. The disturbance can even lead to a complete ejection of the primary's envelope (Ivanova et al., 2013) and, in any case, results in a change in density. Only the formalism of Kim (2010) tries to predict a change in density caused by the companion and, therefore, it is to expect that the absolute change in  $C_d$  is the smallest when using this formalism. For the others (BHL; Ostriker, 1999; Kim & Kim, 2007) it is plausible that there are changes in  $C_d$  for different mass ratios. This is because a more massive companion leads to greater expansion of the envelope which results in a decrease in density. With a lower density, the drag force is lower as well. Therefore, we need a lower  $C_d$  for higher mass ratios to compensate for the decrease in drag force, which is part of the 3D AREPO simulation but not of our semi-analytic approach.

If we switched to a dynamical density profile of the envelope, which changes during the simulation, we would expect the  $C_d$  to stay constant when using the same primary star. And even for different primary stars the  $C_d$  should stay the same if the used drag force is a sufficient description of the physics during a common envelope phase. The  $C_d$  change significantly stronger with the Bondi-Hoyle-Lyttleton formalism than with dynamical friction. Therefore, it is likely that the  $C_d$  with the Bondi-Hoyle-Lyttleton formalism do not only compensate for the assumption of

constant density but also for another dependency that is not captured by this drag force formula, e.g. the scaling with the companion mass. This was also found by Chamandy et al. (2019). Therefore, even when using a dynamical density profile, which would be difficult to implement, the  $C_d$  for the Bondi-Hoyle-Lyttleton drag force would probably still change for different mass ratios. The absolute change of  $C_d$  with the formalisms by Ostriker (1999) and Kim & Kim (2007), however, would likely approach zero. This is because the change is already small and the unconsidered disturbance in density is the biggest dependency  $C_d$  has to compensate for.

## 4.2 Hydrodynamic Drag vs. Dynamical Friction

An ongoing discussion in research is if the drag force in common envelope phases is better described by hydrodynamic drag or by dynamical friction. The former is the one-sided accretion of gas and momentum by the object, here described by the Bondi-Hoyle-Lyttleton formalism. The latter is gravitational focusing of matter into a wake that then decelerates the object, here described by the formalisms of Ostriker (1999), Kim & Kim (2007) and Kim (2010).

In their work, Everson et al. (2020) use the drag coefficients of MacLeod & Ramirez-Ruiz (2015); MacLeod et al. (2017) and De et al. (2020), which are based on Bondi-Hoyle-Lyttleton accretion. Further, they limit the mass ratios such that the Bondi accretion radius of the companion does not exceed the orbital separation at any point during the in-spiral phase. This, however, is what happened in our attempts of using the drag coefficients of MacLeod & Ramirez-Ruiz (2015) for our semi-analytic simulations. Thus, their drag coefficients only worked reasonably for one of our seven simulations. An accretion radius of the companion larger than the primary's radius does not seem physical in our case and generally in the context of a common envelope phase. It indicates a present boundary problem of Bondi-Hoyle-Lyttleton accretion within this framework. Dynamical friction, on the other hand, does not depend on the the Bondi accretion radius and thus avoids this problem.

Since the goal here is to be able to simulate the in-spiral phase of a companion without having a corresponding AREPO simulation, the drag coefficients need to be almost constant when using the same primary star. For the formalisms based on dynamical friction the absolute change in  $C_d$  is smaller than for the formalism based on Bondi-Hoyle-Lyttleton accretion (Table 3.1). This means that interpolating the found  $C_d$  or fitting a function to them would return drag coefficients with smaller absolute errors, when using dynamical friction. Additionally, the arguments from the previous section apply and it seems that the Bondi-Hoyle-Lyttleton formalism does not scale correctly with the companion mass. Therefore, it seems that for our semi-analytic approach, the formalisms that are based on dynamical friction are better suited to capture the in-spiral phase of a companion in a common envelope phase.

## 4.3 The Role of Co-Rotation

While Kramer et al. (2020) and Sand et al. (2020) use a co-rotation equal to 95% of the orbital angular frequency at the beginning of the in-spiral phase, others (e.g. Ginat et al., 2020) use a non-rotating envelope and thereby set this factor to 0%. Our results suggest that the outcome of the common envelope phase does not depend on the degree of co-rotation. It only changes the timescale on which the event plays out. This result, however, is based on the assumption that the envelope rotates with the same angular velocity at every radius, i.e. as a solid body. If this assumption holds, the orbital velocity of the companion becomes large compared to the orbital velocity of the envelope as the separation becomes smaller. Thus, the relative velocity of the companion in the envelope becomes independent of the envelope's velocity for small orbital separations. In other words, the companion's relative velocity becomes independent of co-rotation towards the end of the in-spiral phase.

In reality, the envelope probably does not rotate as a solid body but has a higher angular velocity closer to the core. This implies that the velocity of the envelope is only negligible at even smaller separations when compared to the solid body model. However, the outcome of the common envelope phase still stays unchanged as the relative velocities approach the same value for different degrees of co-rotation. Thus, only the timescale of the event increases for lower co-rotation. We can conclude that by assuming that the envelope is in co-rotation with the companion as a solid body, lower degrees of co-rotation lead to an increased timescale on which the common envelope phase takes place. However, the outcome of the event, i.e. if it approaches a final separation or if the two objects will merge, does not seem to change. In reality, the increase of the the timescale is likely to be even stronger for lower co-rotation.

This also means that using a high degree of co-rotation can save a significant amount of computation time without changing the core features, and especially the outcome, of the simulated common envelope phase. The savings in computation time are already noticeable for our semi-analytic model, where a complete simulation takes minutes at most while running on a single CPU core, and could be drastic for 3D simulations that typically require several hundred thousand CPU-hours per simulation. Future work will explore the significance of this finding.

## 4.4 Outcome of a Common Envelope Event

In Ivanova & Nandez (2016), three possible outcomes of a common envelope event have been stated as follows.

- (i) *Binary formation.* The primary's envelope has been ejected.
- (ii) *Slow spiral-in.* The primary's envelope has not been fully ejected and no further outflow of mass is taking place.
- (iii) *Merger.* The two objects have become one as tidal forces caused material from the companion to be gravitationally bound to the primary.

These follow the definition of Podsiadlowski (2001) and were reviewed in more detail in Ivanova et al. (2013). Since our semi-analytic model assumes a constant density of the primary's envelope, there should be no binary formation possible and even the slow spiral-in is defined to begin after the envelope has, at least, expanded or lost some of its mass as a reaction to the companion moving through it. However, our results also show a slowing-down of the in-spiral phase (e.g. Figure 3.12) and, in parts, even fulfill the criterion for the end of the 'plunge-in phase' (Ivanova & Nandez, 2016), which we refer to as in-spiral phase. This indicates that the expansion of the envelope, especially for small mass ratios, is mainly taking place outside of the companion's orbit. Additionally, on the timescale of the in-spiral phase, the disturbance of the envelope may be negligible for the parts inside of the companion's orbit.

In our setup, the slowing-down is indicated by the ratio of drag force and gravitational force  $F_d/F_g$  approaching zero. This should, therefore, also be the case for 3D simulations as the ones by Kramer et al. (2020) and Sand et al. (2020) since, again, the expansion of the envelope and its ejection is taking place mainly outside of the companion's orbit, while the mass and the density inside the orbit stays approximately constant. Hence, it seems that the expansion and ejection of the primary's envelope is not only a reason for the in-spiral to slow down, but rather a consequence of the in-spiral with repercussions. Further, part of the slowing-down of the in-spiral seems to be due to the gravitational force becoming larger than the drag force by orders of magnitude.

## 5 Conclusion and Outlook

Common envelope phases are important catalysts in the evolution of binary systems. However, modern 3D simulations that include all, or nearly all, of the necessary physics typically require several hundred thousand CPU-hours to cover a complete common envelope phase. The goal of this thesis was to calibrate a semi-analytic model of a common envelope phase to a corresponding 3D simulation. If this was possible with a constant drag coefficient  $C_d$ , the computation time needed for a common envelope simulation could be decreased by orders of magnitude. Instead of several hundred thousand CPU-hours, such a semi-analytic simulation takes minutes at most to run on a single CPU core. To simulate the evolution of orbital separation, we would then only need to numerically solve the equation of motion for a companion on circular orbits with an additional drag force.

The semi-analytic simulations were calibrated to the 3D simulations carried out by Kramer et al. (2020) and Sand et al. (2020) utilizing the moving-mesh magnetohydrodynamics code AREPO. The equations of motion for both primary and companion in the center of mass frame were then derived by adding an additional drag force to the equation of motion for Keplerian (circular) orbits. The drag force was described by four different drag formalisms. One was based on Bondi-Hoyle-Lyttleton accretion and the other three were based on dynamical friction. The equations of motion were solved by applying the numerical RK45 method, also known as Runge-Kutta-Fehlberg method.

In this thesis, we saw that it is, indeed, possible to simulate common envelope phases with a 1D semi-analytic approach and still achieve a high degree of accuracy. For predicting the timescale on which the common envelope phase plays out, this approach seems to be absolutely applicable. However, the outcome of the common envelope phase still remained somewhat arbitrary and depended heavily on the used formalism. And while it is clear to say that the formalism of Kim (2010) was the best to match the course of the common envelope phase for more massive companions, it was not the best for smaller mass ratios. There, the formalism of Kim & Kim (2007) was superior. Nevertheless, we found that for the in-spiral phase of the companion to end, the ratio  $F_d/F_g$  must approach zero. Only then does the drag force become negligible compared to the gravitational force and has no significant influence of the total change of the companion's velocity any more. Furthermore, we defined the timescale  $\tau_{\text{in}}/P_0$  which expresses how long it would take to remove all of the angular momentum from the companion with the current drag force. We found that  $\tau_{\text{in}}/P_0$  always showed a minimum if the semi-analytic simulation approached a final

separation of primary and companion where the companion does not seem to advance deeper into the primary over a long period. The timescale from Ivanova & Nandez (2016), which is supposed to characterize the end of the in-spiral if  $r/|\dot{r}P| > 10$ , does also apply for many of our semi-analytic simulations and therefore seems to be chosen reasonably.

Another insight that was obtained and could have implications for future common envelope simulations is related to the choice of the initial co-rotation in the binary system. We found that the degree of co-rotation between companion and the primary's envelope does not change the outcome of the common envelope phase but only the time scale on which it takes place. More specifically, a higher degree of co-rotation, i.e. more similar angular velocities of companion and envelope, led to a faster in-spiral but approached the same final separation as the same simulation with a different degree of co-rotation. This is an important finding as it could help to save a significant amount of computation time for common envelope simulations by simply adjusting one initial parameter.

By comparing the Bondi-Hoyle-Lyttleton drag formalism to three formalisms that are based on dynamical friction, it became apparent that dynamical friction is more suited for usage in the framework of a common envelope phase. Further, it is necessary to account for circular orbits (Kim & Kim, 2007) and also for non-linear perturbation (Kim, 2010) (in the case of high mass ratios) when trying to simulate a common envelope phase with a semi-analytic model and good accuracy. We found that none of these formalisms could be calibrated with constant  $C_d$ . This is not necessarily due to the assumption of constant density, as it was discussed in Chapter 4, but indicates that there is still a better choice for the Coulomb logarithm to find. In practice, this means that  $C_d$  would have to be guessed accordingly when trying to simulate a common envelope phase with a primary star or a mass ratio that differs from those that were part of this work.

The work of MacLeod & Ramirez-Ruiz (2015) was also applied to our semi-analytic simulations. With the help of a wind tunnel experiment simulated in 3D, the authors were able to determine a fit formula for the drag coefficients  $C_d$  in a Bond-Hoyle-Lyttleton framework. The formula was then used to provide  $C_d$  for our simulations. However, only for the two smallest mass ratios the provided  $C_d$  resulted in an acceptable solution. This incompatibility was probably due to differences in the setup of the experiments. In their work, MacLeod & Ramirez-Ruiz (2015) only studied cases with Mach numbers of  $\mathcal{M} = 1.1, 2, 3$  but in our simulations the Mach number could also decrease below one. This led to the  $C_d$  provided by the fit formula generally being too high.

In future work, 3D simulations with AREPO will be made to verify the finding that the initial co-rotation changes only the timescale of the common envelope phase and not the outcome. For this, the model of Kramer et al. (2020) will be modified for different degrees of co-rotation. Hopefully, Figure 3.16 can be recreated with the resulting AREPO data. This will show if there are savings in computation time to be made and also how good the semi-analytic model is in predicting the course of a

common envelope phase.

Additionally, the calibration could be carried out for more than seven different mass ratios. With more data points, we could establish a fit formula similar to the approach of MacLeod & Ramirez-Ruiz (2015) to provide a better basis for semi-analytic common envelope phases.

For now, all of the code for our semi-analytic simulation was written in Python. Even though the simulations took minutes, at most, possibly some time savings could be achieved by translating the code into a compiled language like, for example, Fortran. When written in Fortran, the routine could also be, at some point, implemented into the stellar evolution code MESA. This would be an easy way to make fast, yet accurate, 1D simulations for common envelope simulations. Natively implemented into MESA, the routine could then be used to quickly simulate a common envelope phase for any evolved primary star. With some modifications it would also be possible to take the expanding envelope into account when using updated MESA profiles during the semi-analytic simulation. This could increase the accuracy of the simulation even further.

## 6 Acknowledgments

I would like to express my thanks to Dr. Fabian Schneider for offering me the possibility to write this thesis under his supervision. I am grateful for his continued help and support during my time as a member of his research group Stellar Evolution Theory (SET) at Heidelberg Institute for Theoretical Studies (HITS).

Further, I want to thank Prof. Dr. Friedrich Röpke, leader of the research group Physics of Stellar Objects (PSO) at HITS, for being the second referee for this thesis. I am also thankful for the opportunity he gave me to do an internship in his group prior to my thesis.

I would like to thank Christian Sand, who was always there to help me if I had any problems regarding the computational parts of my thesis or with anything else - even on weekends. I am also grateful for all the other members of the PSO and SET groups. They provided helpful comments and ideas to improve my work. Working alongside them was a pleasure.

Finally, I want to thank my friends and family for their continued trust and support during the time this thesis was written.

## A Additional Figures

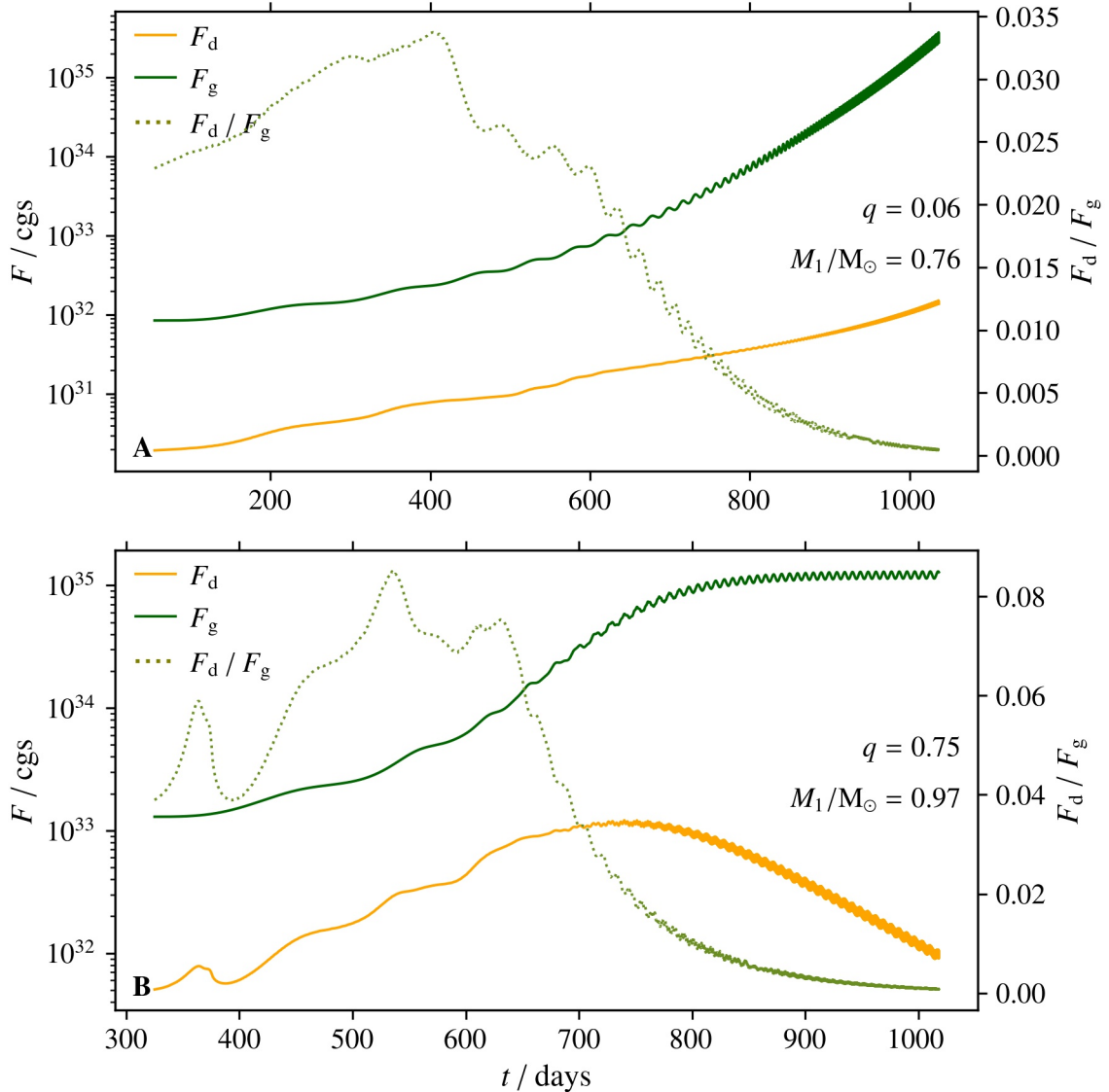


**Figure A.1: BHL.** The drag force is plotted as orange solid line. The gravitational force is plotted as green solid line. Their ratio is plotted as a green dotted line. **A:**  $0.76 M_\odot$  RGB primary star and mass ratio of  $M_2/M_1 = 0.06$ . **B:**  $0.97 M_\odot$  AGB primary star and mass ratio of  $M_2/M_1 = 0.75$ .

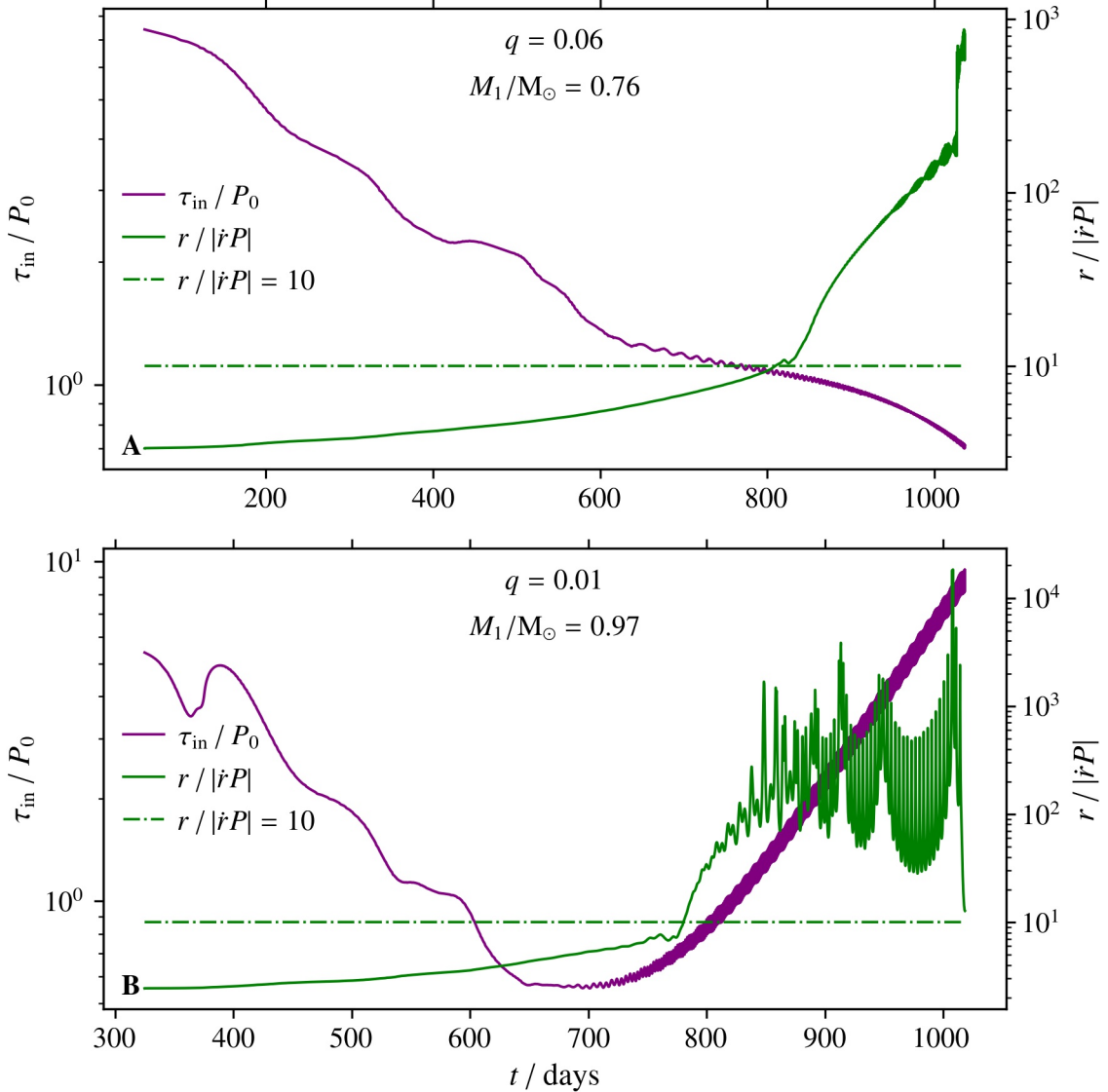


**Figure A.2: BHL.** The angular momentum timescale is plotted as a purple solid line. The orbital separation timescale (Ivanova & Nandez, 2016) is plotted as a green solid line. The threshold which indicates the end of the in-spiral phase is plotted as green dashed-dotted line. **A:**  $0.76 M_\odot$  RGB primary star and mass ratio of  $M_2/M_1 = 0.06$ . **B:**  $0.97 M_\odot$  AGB primary star and mass ratio of  $M_2/M_1 = 0.75$ .

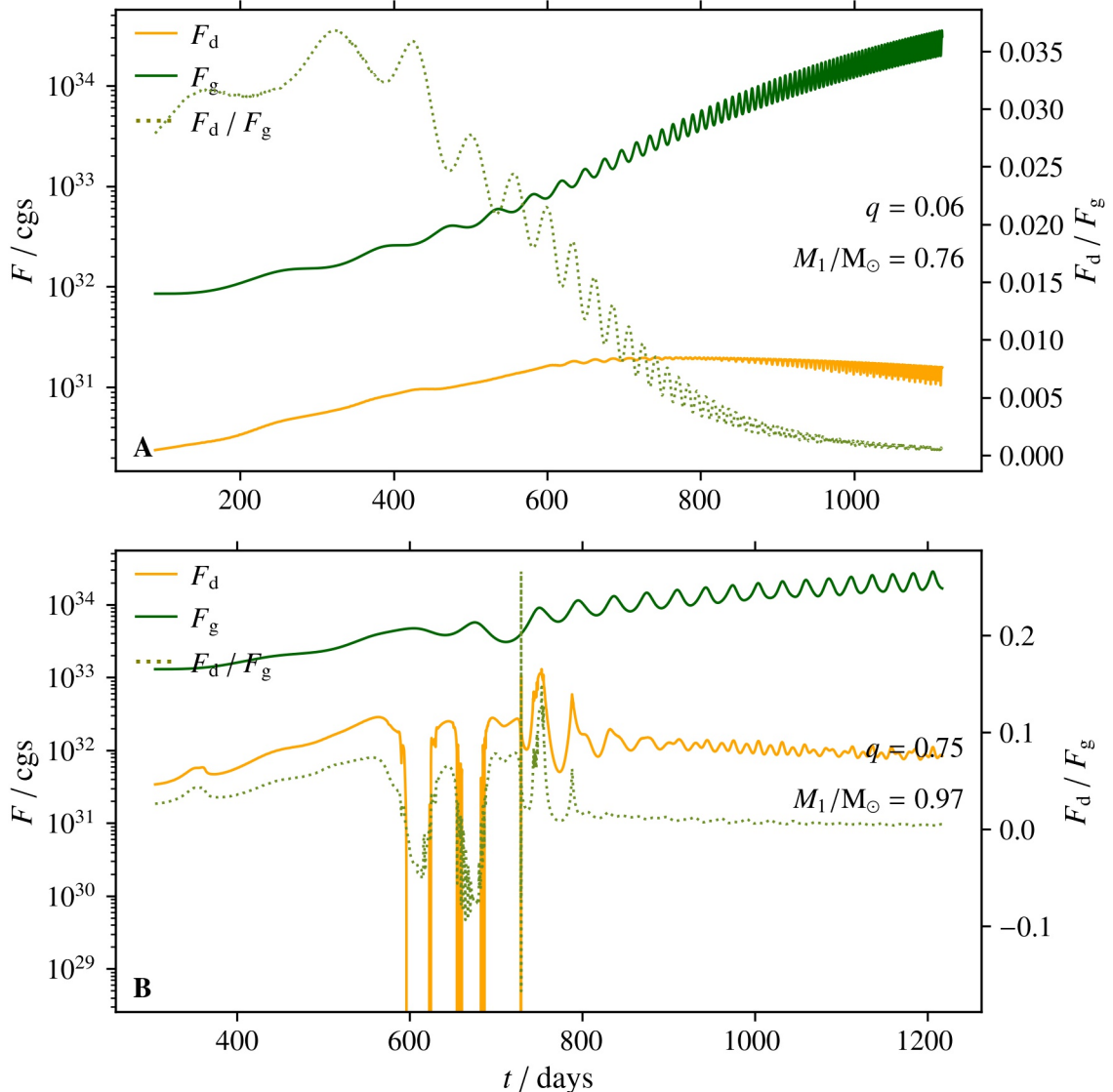


**Figure A.3:** O99. The drag force is plotted as orange solid line. The gravitational force is plotted as green solid line. Their ratio is plotted as a green dotted line. **A:**  $0.76 M_\odot$  RGB primary star and mass ratio of  $M_2/M_1 = 0.06$ . **B:**  $0.97 M_\odot$  AGB primary star and mass ratio of  $M_2/M_1 = 0.75$ .

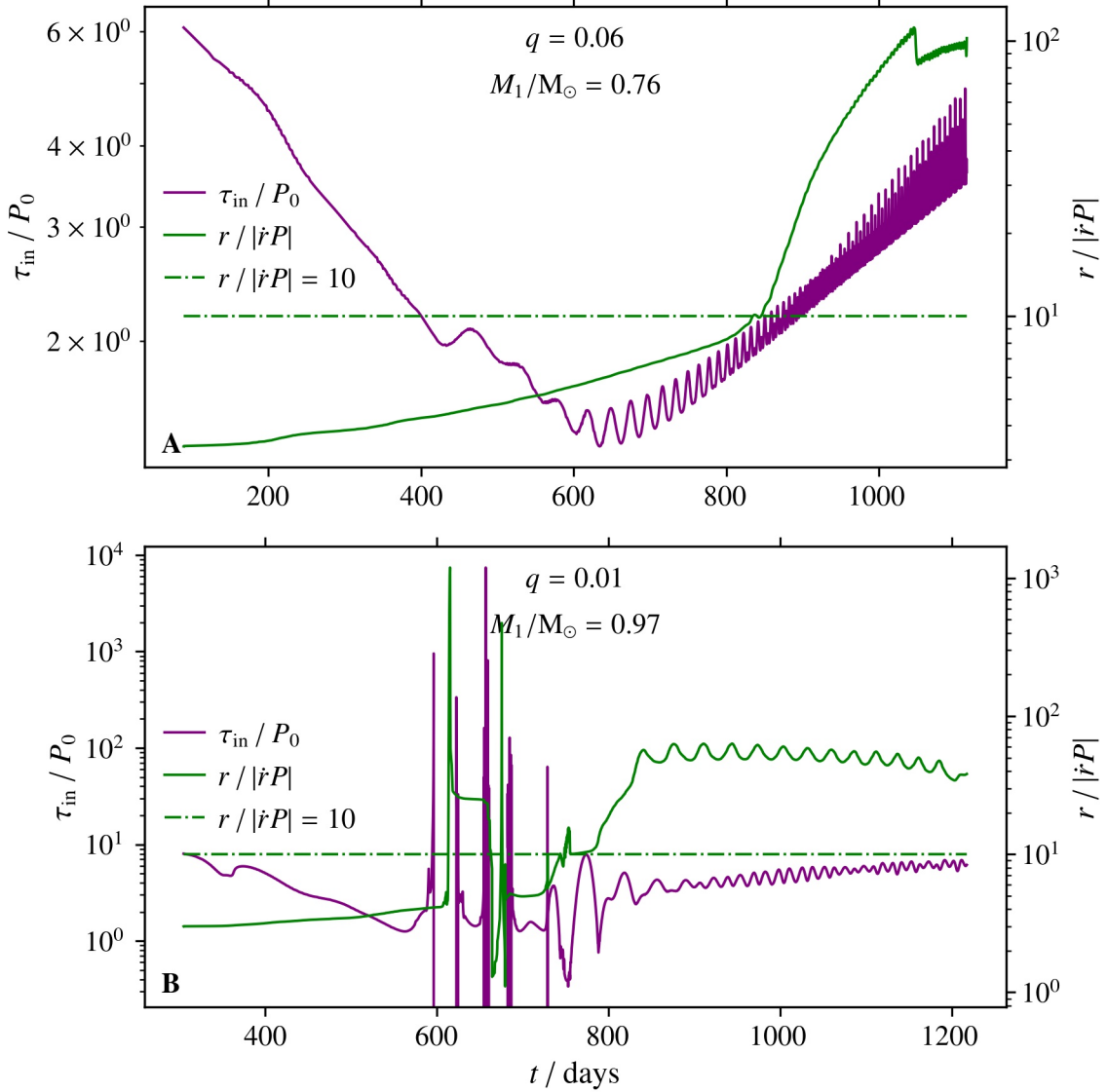


**Figure A.4:** O99. The angular momentum timescale is plotted as a purple solid line. The orbital separation timescale (Ivanova & Nandez, 2016) is plotted as a green solid line. The threshold which indicates the end of the in-spiral phase is plotted as green dashed-dotted line. **A:**  $0.76 M_\odot$  RGB primary star and mass ratio of  $M_2/M_1 = 0.06$ . **B:**  $0.97 M_\odot$  AGB primary star and mass ratio of  $M_2/M_1 = 0.75$ .

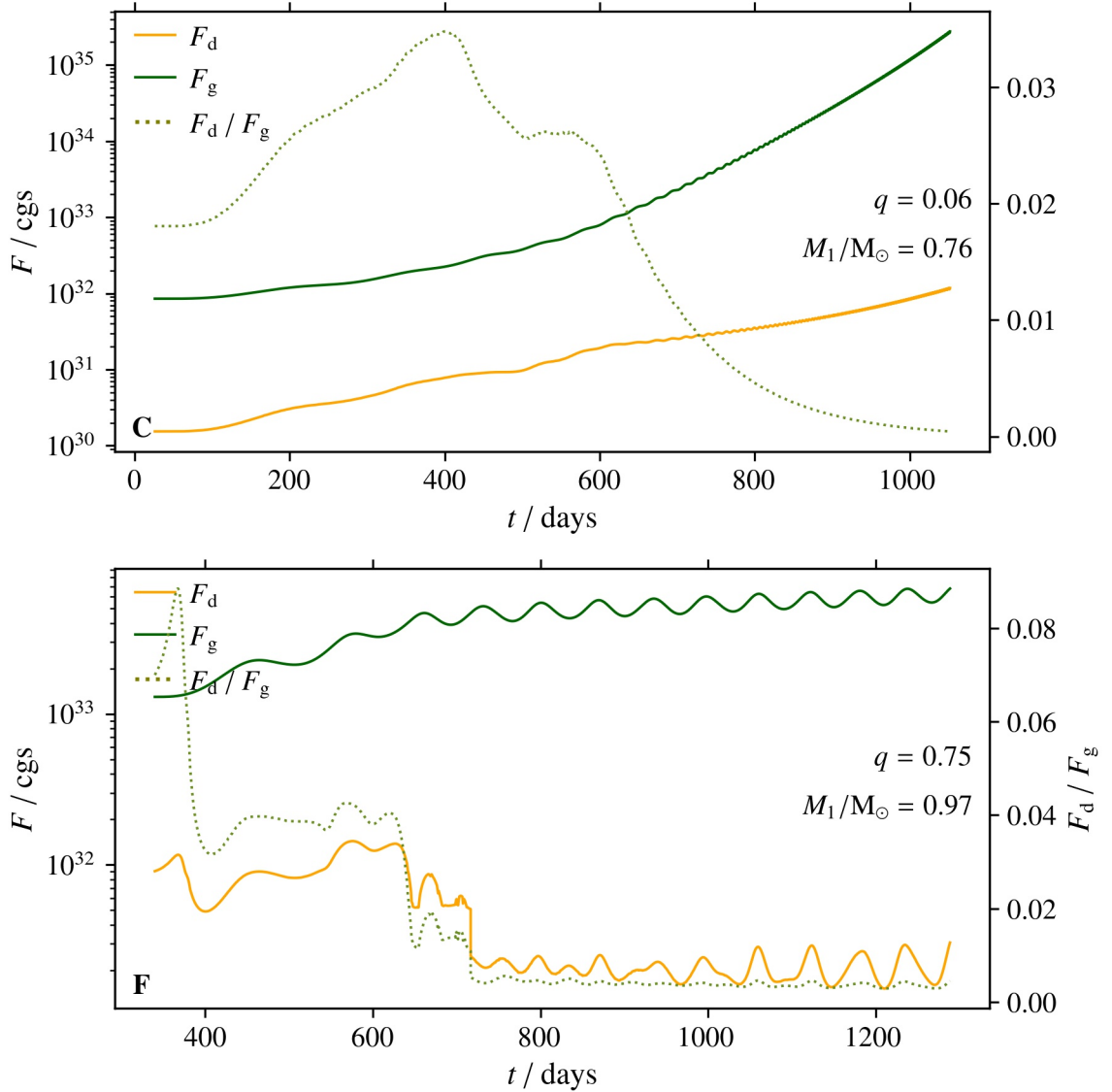


**Figure A.5: K10.** The drag force is plotted as orange solid line. The gravitational force is plotted as green solid line. Their ratio is plotted as a green dotted line. **A:**  $0.76 M_\odot$  RGB primary star and mass ratio of  $M_2/M_1 = 0.06$ . **B:**  $0.97 M_\odot$  AGB primary star and mass ratio of  $M_2/M_1 = 0.75$ .

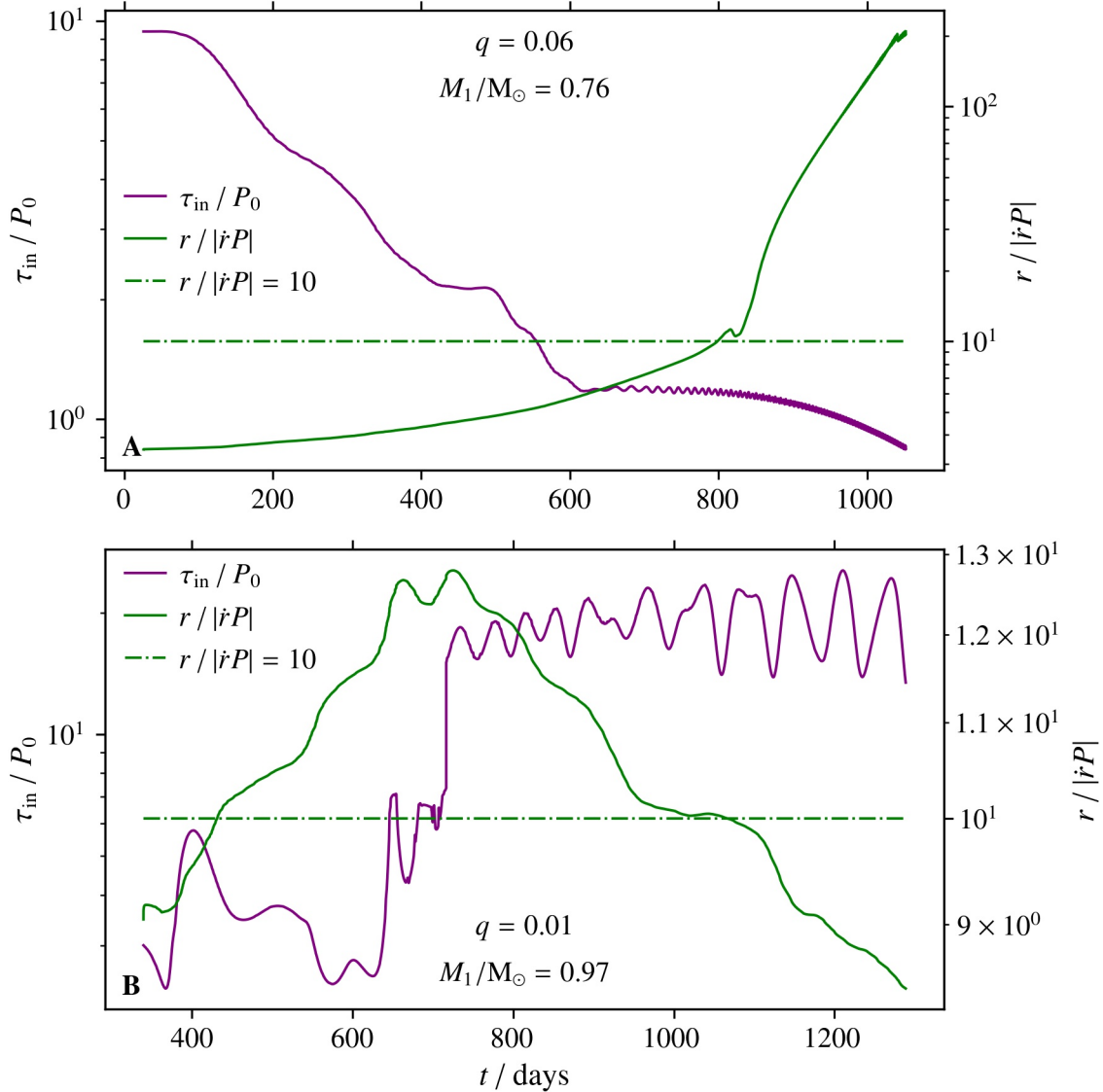


**Figure A.6:** K10. The angular momentum timescale is plotted as a purple solid line. The orbital separation timescale (Ivanova & Nandez, 2016) is plotted as a green solid line. The threshold which indicates the end of the in-spiral phase is plotted as green dashed-dotted line. **A:**  $0.76 M_\odot$  RGB primary star and mass ratio of  $M_2/M_1 = 0.06$ . **B:**  $0.97 M_\odot$  AGB primary star and mass ratio of  $M_2/M_1 = 0.75$ .

## B Lists

### B.1 List of Figures

1.1	Exerted drag force on a companion that travels through a gaseous medium as function of Mach number. The formalism of Kim & Kim (2007) is plotted as a black solid line and is in good agreement with the formalism of Ostriker (1999) which is plotted as orange dotted line. Additionally, the Bondi-Hoyle-Lyttleton formalism is plotted as green dashed-dotted line. . . . .	14
3.1	Position in the $xy$ -plane of the primary star as orange dotted line (hardly moves because of the small mass ratio) and the companion as blue solid line over the course of the in-spiral phase for $q = 0.01$ with a drag force described by Bondi-Hoyle-Lyttleton accretion. . . . .	24
3.2	Separation of primary star and companion for $q = 0.01$ as a function of time with a drag force described by Bondi-Hoyle-Lyttleton accretion as blue solid line compared to the corresponding 3D-simulation with AREPO as orange dashed-dotted line. The tidal disruption radius is plotted as grey dotted line. . . . .	25
3.3	Relative velocity of the companion in the gas of the envelope as blue solid line, sound speed as brown solid line and Mach number as purple dotted line for $q = 0.01$ as a function of time with a drag force described by Bondi-Hoyle-Lyttleton accretion. . . . .	26
3.4	Drag force as orange solid line, gravitational force as green solid line and their ratio as green dotted line for $q = 0.01$ as a function of time with a drag force described by Bondi-Hoyle-Lyttleton accretion. . . . .	27
3.5	Separation of primary star and companion for $q = 0.01\text{-}0.10$ , $M_1 = 0.76 M_\odot$ and $q = 0.25\text{-}0.75$ , $M_1 = 0.97 M_\odot$ as a function of time with a drag force described by Bondi-Hoyle-Lyttleton accretion. The grey marked part is where the companion moves sub-sonically through the envelope. . . . .	28
3.6	Separation of primary star and companion for $q = 0.01$ as a function of time with a drag force described by Bondi-Hoyle-Lyttleton accretion. The results of AREPO are additionally plotted with an offset of $n \cdot r_{\text{fin}}$ for $n = 1, 2, 3, 4, 5$ in dotted lines of different colors. . . . .	29
3.7	Separation of primary star and companion for $q = 0.01, 0.04$ as a function of time with $C_d$ from MacLeod & Ramirez-Ruiz (2015). . . . .	30

3.8	Velocities (A) and exerted forces (B) over time for $q = 0.06$ with $C_d$ from MacLeod & Ramirez-Ruiz (2015). . . . .	31
3.9	Separation of primary star and companion for $q = 0.01\text{-}0.10$ , $M_1 = 0.76 M_\odot$ and $q = 0.25\text{-}0.75$ , $M_1 = 0.97 M_\odot$ as a function of time with a drag force as in Ostriker (1999). . . . .	32
3.10	Velocities (A) and exerted forces (B) over time for $q = 0.75$ with a drag force as in Ostriker (1999). . . . .	34
3.11	Separation of primary star and companion for $q = 0.01$ as a function of time with a drag force as in Ostriker (1999). The results of AREPO are additionally plotted with an offset of $n \cdot r_{\text{fin}}$ for $n = 1, 2, 3, 4, 5$ in dotted lines of different colors. . . . .	35
3.12	Separation of primary star and companion for $q = 0.01\text{-}0.10$ , $M_1 = 0.76 M_\odot$ and $q = 0.25\text{-}0.75$ , $M_1 = 0.97 M_\odot$ as a function of time with a drag force as in Kim & Kim (2007). . . . .	36
3.13	Separation of primary star and companion for $q = 0.01$ as a function of time with a drag force as in Kim & Kim (2007). The results of AREPO are additionally plotted with an offset of $n \cdot r_{\text{fin}}$ for $n = 1, 2, 3, 4, 5$ in dotted lines of different colors. . . . .	37
3.14	Separation of primary star and companion for $q = 0.01\text{-}0.10$ , $M_1 = 0.76 M_\odot$ and $q = 0.25\text{-}0.75$ , $M_1 = 0.97 M_\odot$ as a function of time with a drag force as in Kim (2010). . . . .	38
3.15	Separation of primary star and companion for $q = 0.01$ as a function of time with a drag force as in Kim (2010). The results of AREPO are additionally plotted with an offset of $n \cdot r_{\text{fin}}$ for $n = 1, 2, 3, 4, 5$ in dotted lines of different colors. . . . .	39
3.16	Separation of primary star and companion for $q = 0.01$ as a function of time with a drag force as in Kim & Kim (2007) for different initial co-rotation. . . . .	41
3.17	Mach number as a function of orbital separation of primary star and companion for different initial co-rotation. . . . .	42
3.18	Angular momentum timescale in purple and orbital separation timescale in green. The limit which indicates the end of the in-spiral (Ivanova & Nandez, 2016) is plotted as green dashed-dotted line. . . . .	44
A.1	<i>BHL</i> . The drag force is plotted as orange solid line. The gravitational force is plotted as green solid line. Their ratio is plotted as a green dotted line. <b>A</b> : $0.76 M_\odot$ RGB primary star and mass ratio of $M_2/M_1 = 0.06$ . <b>B</b> : $0.97 M_\odot$ AGB primary star and mass ratio of $M_2/M_1 = 0.75$ . . . . .	54
A.2	<i>BHL</i> . The angular momentum timescale is plotted as a purple solid line. The orbital separation timescale (Ivanova & Nandez, 2016) is plotted as a green solid line. The threshold which indicates the end of the in-spiral phase is plotted as green dashed-dotted line. <b>A</b> : $0.76 M_\odot$ RGB primary star and mass ratio of $M_2/M_1 = 0.06$ . <b>B</b> : $0.97 M_\odot$ AGB primary star and mass ratio of $M_2/M_1 = 0.75$ . . . . .	55

A.3	<i>O99.</i> The drag force is plotted as orange solid line. The gravitational force is plotted as green solid line. Their ratio is plotted as a green dotted line. <b>A:</b> $0.76 M_{\odot}$ RGB primary star and mass ratio of $M_2/M_1 = 0.06$ . <b>B:</b> $0.97 M_{\odot}$ AGB primary star and mass ratio of $M_2/M_1 = 0.75$ .	56
A.4	<i>O99.</i> The angular momentum timescale is plotted as a purple solid line. The orbital separation timescale (Ivanova & Nandez, 2016) is plotted as a green solid line. The threshold which indicates the end of the in-spiral phase is plotted as green dashed-dotted line. <b>A:</b> $0.76 M_{\odot}$ RGB primary star and mass ratio of $M_2/M_1 = 0.06$ . <b>B:</b> $0.97 M_{\odot}$ AGB primary star and mass ratio of $M_2/M_1 = 0.75$ .	57
A.5	<i>K10.</i> The drag force is plotted as orange solid line. The gravitational force is plotted as green solid line. Their ratio is plotted as a green dotted line. <b>A:</b> $0.76 M_{\odot}$ RGB primary star and mass ratio of $M_2/M_1 = 0.06$ . <b>B:</b> $0.97 M_{\odot}$ AGB primary star and mass ratio of $M_2/M_1 = 0.75$ .	58
A.6	<i>K10.</i> The angular momentum timescale is plotted as a purple solid line. The orbital separation timescale (Ivanova & Nandez, 2016) is plotted as a green solid line. The threshold which indicates the end of the in-spiral phase is plotted as green dashed-dotted line. <b>A:</b> $0.76 M_{\odot}$ RGB primary star and mass ratio of $M_2/M_1 = 0.06$ . <b>B:</b> $0.97 M_{\odot}$ AGB primary star and mass ratio of $M_2/M_1 = 0.75$ .	59

## B.2 List of Tables

3.1	Determined $C_d$ for different $q$ with drag forces from all discussed formalisms. BHL: Bondi-Hoyle-Lyttleton; O99: Ostriker (1999); KK07: Kim & Kim (2007); K10: Kim (2010)	40
-----	--	----

## C Bibliography

- Belczynski K., Kalogera V., Bulik T., 2002, *ApJ*, 572, 407
- Bermúdez-Bustamante L. C., García-Segura G., Steffen W., Sabin L., 2020, *MNRAS*, 493, 2606
- Chabrier G., Baraffe I., Allard F., Hauschildt P., 2000, *The Astrophysical Journal*, 542, 464
- Chamandy L., Blackman E. G., Frank A., Carroll-Nellenback J., Zou Y., Tu Y., 2019, *MNRAS*, 490, 3727
- Chandrasekhar S., 1943, *ApJ*, 97, 255
- Clayton M., Podsiadlowski P., Ivanova N., Justham S., 2017, *MNRAS*, 470, 1788
- De S., MacLeod M., Everson R. W., Antoni A., Mandel I., Ramirez-Ruiz E., 2020, *ApJ*, 897, 130
- Dokuchaev V. P., 1964, *Soviet Ast.*, 8, 23
- Edgar R., 2004, *New A Rev.*, 48, 843
- Eggleton P. P., 1983, *ApJ*, 268, 368
- Escala A., Larson R. B., Coppi P. S., Mardones D., 2004, *ApJ*, 607, 765
- Everson R. W., MacLeod M., De S., Macias P., Ramirez-Ruiz E., 2020, *ApJ*, 899, 77
- Fragos T., Andrews J. J., Ramirez-Ruiz E., Meynet G., Kalogera V., Taam R. E., Zezas A., 2019, *ApJ*, 883, L45
- Ginat Y. B., Glanz H., Perets H. B., Grishin E., Desjacques V., 2020, *MNRAS*, 493, 4861
- Iben I. J., Tutukov A. V., 1984, *ApJS*, 54, 335
- Ivanova N., 2002, PhD thesis, Univ. Oxford
- Ivanova N., Nandez J. L. A., 2016, *MNRAS*, 462, 362
- Ivanova N., et al., 2013, *A&A Rev.*, 21, 59
- Kim W.-T., 2010, *ApJ*, 725, 1069

- Kim H., Kim W.-T., 2007, *ApJ*, 665, 432
- Kramer M., Schneider F. R. N., Ohlmann S. T., Geier S., Schaffenroth V., Pakmor R., Röpke F. K., 2020, *A&A*, 642, A97
- Lada C. J., 2006, *ApJ*, 640, L63
- Livio M., Shankar A., Burkert A., Truran J. W., 1990, *ApJ*, 356, 250
- MacLeod M., Ramirez-Ruiz E., 2015, *ApJ*, 803, 41
- MacLeod M., Antoni A., Murguia-Berthier A., Macias P., Ramirez-Ruiz E., 2017, *ApJ*, 838, 56
- Meyer F., Meyer-Hofmeister E., 1979, *A&A*, 78, 167
- Nandez J. L. A., Ivanova N., Lombardi J. C. J., 2015, *MNRAS*, 450, L39
- Nordhaus J., Blackman E. G., Frank A., 2007, *MNRAS*, 376, 599
- Ohlmann S. T., Röpke F. K., Pakmor R., Springel V., 2016, *ApJ*, 816, L9
- Ostriker E. C., 1999, *ApJ*, 513, 252
- Paczynski B., 1976, in Eggleton P., Mitton S., Whelan J., eds, Vol. 73, Structure and Evolution of Close Binary Systems. p. 75
- Pakmor R., Kromer M., Röpke F. K., Sim S. A., Ruiter A. J., Hillebrandt W., 2010, *Nature*, 463, 61
- Passy J.-C., et al., 2012, *ApJ*, 744, 52
- Paxton B., Bildsten L., Dotter A., Herwig F., Lesaffre P., Timmes F., 2011, *ApJS*, 192, 3
- Pejcha O., Metzger B. D., Tomida K., 2016a, *MNRAS*, 455, 4351
- Pejcha O., Metzger B. D., Tomida K., 2016b, *MNRAS*, 461, 2527
- Podsiadlowski P., 2001, in Podsiadlowski P., Rappaport S., King A. R., D'Antona F., Burderi L., eds, Astronomical Society of the Pacific Conference Series Vol. 229, Evolution of Binary and Multiple Star Systems. p. 239
- Rephaeli Y., Salpeter E. E., 1980, *ApJ*, 240, 20
- Ricker P. M., Taam R. E., 2008, *ApJ*, 672, L41
- Ricker P. M., Taam R. E., 2012, *ApJ*, 746, 74
- Ruderman M. A., Spiegel E. A., 1971, *ApJ*, 165, 1

- Ruiter A. J., Belczynski K., Fryer C., 2009, *ApJ*, 699, 2026
- Ruiter A. J., et al., 2013, *MNRAS*, 429, 1425
- Sánchez-Salcedo F. J., Brandenburg A., 2001, *MNRAS*, 322, 67
- Sand C., Ohlmann S. T., Schneider F. R. N., Pakmor R., Röpke F. K., 2020, *A&A*, 644, A60
- Shu F. H., 1982, The Physical Universe: an Introduction to Astronomy. University Science Books
- Taam R. E., 1979, *Astrophys. Lett.*, 20, 29
- Taam R. E., Ricker P. M., 2010, *New Astronomy Reviews*, 54, 65
- Taam R. E., Bodenheimer P., Ostriker J. P., 1978, *ApJ*, 222, 269
- de Kool M., 1990, *ApJ*, 358, 189

# Erklärung

Ich versichere, dass ich diese Arbeit selbstständig verfasst und keine anderen als die angegebenen Quellen und Hilfsmittel benutzt habe.

Heidelberg, den 22.04.2021, L.Thümler